

1 **A machine learning approach to tungsten prospectivity modelling using** 2 **knowledge-driven feature extraction and model confidence**

3 Christopher M. Yeomans^{a,b,*}, Robin K. Shail^a, Stephen Grebby^c, Vesa Nykänen^d,

4 Maarit Middleton^d and Paul A.J. Lusty^b

5 ^aCamborne School of Mines, College of Engineering, Mathematics and Physical Sciences, University of Exeter,
6 Penryn Campus, Penryn, Cornwall, TR10 9FE, UK

7 ^bBritish Geological Survey, Environmental Science Centre, Keyworth, Nottinghamshire, NG12 5GG, UK

8 ^cUniversity of Nottingham, Nottingham Geospatial Institute, Innovation Park, Nottingham, NG7 2TU, UK

9 ^dGeological Survey of Finland, P.O. Box 77, FI-96101, Rovaniemi, Finland

10

11 *Keywords*

12 Machine learning; Mineral prospectivity modelling; Mineral exploration; Random Forest™; Tungsten;
13 SW England

14

15 **Abstract**

16 Novel mineral prospectivity modelling presented here applies knowledge-driven feature extraction to a
17 data-driven machine learning approach for tungsten mineralisation. The method emphasises the
18 importance of appropriate model evaluation and develops a new Confidence Metric to generate
19 spatially refined and robust exploration targets. The data-driven Random Forest™ algorithm is
20 employed to model tungsten mineralisation in SW England using a range of geological, geochemical
21 and geophysical evidence layers which include a depth to granite evidence layer. Two models are
22 presented, one using standardised input variables and a second that implements fuzzy set theory as
23 part of an augmented feature extraction step. The use of fuzzy data transformations mean feature
24 extraction can incorporate some user-knowledge about the mineralisation into the model. The
25 typically subjective approach is guided using the Receiver Operating Characteristics (ROC) curve tool
26 where transformed data are compared to known training samples. The modelling is conducted using
27 34 known true positive samples with 10 sets of randomly generated true negative samples to test the
28 random effect on the model. The two models have similar accuracy but show different spatial
29 distributions when identifying highly prospective targets. Areal analysis shows that the fuzzy-
30 transformed model is a better discriminator and highlights three areas of high prospectivity that were
31 not previously known. The Confidence Metric, derived from model variance, is employed to further
32 evaluate the models. The new metric is useful for refining exploration targets and highlighting the
33 most robust areas for follow-up investigation. The fuzzy-transformed model is shown to contain larger
34 areas of high model confidence compared to the model using standardised variables. Finally, legacy
35 mining data, from drilling reports and mine descriptions, is used to further validate the fuzzy-

36 transformed model and gauge the depth of potential deposits. Descriptions of mineralisation
37 corroborate that the targets generated in these models could be undercover at depths of less than
38 300 m. In summary, the modelling workflow presented herein provides a novel integration of
39 knowledge-driven feature extraction with data-driven machine learning modelling, while the newly
40 derived Confidence Metric generates reliable mineral exploration targets.

41

42 1. Introduction

43 The use of Machine Learning Algorithms (MLAs) for mineral prospectivity modelling has
44 been driven by the increasing size of individual datasets and the range of data types
45 available for mineral exploration. MLAs are computationally efficient and can deal with
46 large, high-dimensional input datasets, non-Gaussian distributions, and generate robust
47 exploration targets from few training samples (Carranza and Laborte, 2015a, 2015b;
48 Rodriguez-Galiano et al., 2015). The approach requires some *a priori* data to train the
49 model, indicating that it is a data-driven method. However, the number of training samples
50 can be <20 which is a significant improvement compared to other data-driven methods such
51 as Weights-of-Evidence (Carranza and Laborte, 2015b). MLAs are now commonplace in
52 mineral prospectivity modelling. The Random Forest, Support Vector Machine and Artificial
53 Neural Network algorithms are regularly implemented and it is the Random Forest MLA that
54 is proving most effective in comparison studies (Rodriguez-Galiano et al., 2015; Sun et al.,
55 2019).

56 Prospectivity modelling is often conducted at a large-scale, encompassing national or
57 regional areas to determine new exploration targets. Studies have become increasingly
58 effective due to investment in the acquisition of high-resolution airborne geophysical,
59 satellite and geochemical datasets over large areas (Kreuzer et al., 2010; Bahiru and Woldai,
60 2016). Furthermore, the commitment from national geological surveys to undertake
61 airborne geophysical surveys and geochemical baseline studies for both mineral exploration
62 and environmental purposes has led to high-quality datasets often being freely available.

63 Classical prospectivity modelling has been dominated by the Weights-of-Evidence and Fuzzy
64 Logic methods. MLAs are a more effective data-driven method compared to Weights-of-
65 Evidence but are dependent on an effective set of training data and their ability to
66 generalise unseen data when defining new deposits. The Fuzzy Logic technique is
67 knowledge-based and founded on fuzzy set theory. The approach allows user-knowledge to
68 be incorporated into the model through various data transformations chosen by the user
69 (Zadeh, 1965; An et al., 1991; Bonham-Carter, 1994). The advantage of this is the ability to
70 weight different data and to introduce some dependencies between variables that may be
71 inferred by the user but not captured in the data within a conceptual deposit model. Until
72 recently, this technique has been considered highly subjective, but work by Nykänen et al.
73 (2015, 2017) provides a means of guiding the data processing by iteratively tuning evidence
74 layers using an evaluation metric. Another method by Burkin et al. (2019) incorporates
75 feature evidence into the initial evidence layer to mitigate interpretative bias of the
76 conceptual model by the user. This approach allows multiple evidence layers to be produced
77 from the same data – mimicking the interpretation of several users – and subsequently

78 combines these through an objective approach (Burkin et al., 2019). The quantitative
79 approach of the former and qualitative approach of the latter are often complementary
80 during feature extraction. In this study we use fuzzy transformations as part of the feature
81 extraction step in MLA modelling. We take the approach of Nykänen et al. (2015, 2017) to
82 ensure the user-knowledge that is introduced to potentially improve a data-driven analysis
83 is quantifiable.

84 MLAs also offer key post-hoc metrics to evaluate the model beyond the standard accuracy
85 metrics. These include model variance and information entropy, which have been
86 investigated, respectively, by Cracknell and Reading (2013) and Kuhn et al. (2018). Cracknell
87 and Reading (2013) demonstrated the value of assessing model variance for a multi-class
88 problem when mapping lithology to highlight fault zones, whereas Kuhn et al. (2018) used
89 information entropy to guide field sampling campaigns to assist with geological mapping.
90 These metrics are useful for highlighting potentially erroneous aspects of a model, which
91 cannot be found when evaluation is based on a single accuracy metric, but have not been
92 implemented within a mineral prospectivity modelling framework.

93 Herein, we demonstrate the use of fuzzy set theory for feature extraction, as well as post-
94 hoc metrics, for tungsten mineralisation in SW England using a Random Forest MLA. We
95 explore how incorporating knowledge-driven principles as part of feature extraction within
96 a data-driven modelling workflow can improve the final results and compare this to a model
97 using standardised (zero mean and equal variance) input variables. Furthermore, the models
98 are spatially evaluated using model variance and a newly derived Confidence Metric which
99 are applied to generate robust targets for mineral exploration with a refined area. Finally,
100 legacy mining data are used to further validate new targets and give a depth estimate to
101 mineralisation.

102 1.1. Geological framework

103 SW England is a world-class tin-tungsten province and provides an excellent case study
104 location for prospectivity modelling due to the recent acquisition of high-resolution airborne
105 geophysical and geochemical datasets (Beamish et al., 2014; British Geological Survey,
106 2016). The regional geology (Figure 1) is dominated by low-grade regionally
107 metamorphosed Devonian-Carboniferous successions that were deformed during the
108 Variscan Orogeny; these were subsequently intruded by the Early Permian Cornubian
109 Batholith (Leveridge and Hartley, 2006; Scrivener, 2006; Shail and Leveridge, 2009; Simons
110 et al., 2016). The batholith is closely associated with a tin-tungsten orefield that has also
111 been exploited for copper, zinc, lead, silver, antimony, arsenic, uranium and a number of
112 other subordinate metals (Jackson et al., 1989). Tungsten vein mineralisation was governed
113 by the coeval post-Variscan regional tectonic and structural development and magmatic and
114 magmatic-hydrothermal evolution of the batholith; these are outlined briefly below.

115 1.1.1. Regional tectonics and structural geology

116 The regional structural geological evolution records two episodes of deformation (D1 and
117 D2) relating to Variscan convergence and continental collision, e.g. Sanderson and Dearman
118 (1973); Rattey and Sanderson (1984); Alexander and Shail (1996). These were associated
119 with the development of NNW-directed thrust faults and NNW-SSE transfer faults within

120 Devonian and Carboniferous successions (Dearman, 1963, 1970; Coward and Smallwood,
121 1984; Shail and Alexander, 1997).

122 Post-convergence NNW-SSE extension (D3) commenced in the latest Carboniferous and
123 brought about reactivation of Variscan thrust faults. Continued extension generated new
124 higher angle extensional faults through much of the Early Permian (Figure 2; Shail and
125 Wilkinson, 1994; Alexander and Shail, 1995, 1996). Subsequent minor, Permian, ENE-WSW
126 (D4) and NNW-SSE (D5) intraplate shortening events are also recognised (Hobson and
127 Sanderson, 1983; Rattey and Sanderson, 1984; Shail and Alexander, 1997). The D3-D5
128 events spanned batholith construction and mineralisation and their brittle expression, as
129 faults and tensile fractures, were essential for the migration of magmatic-hydrothermal
130 fluids and the development of lodes and sheeted veins (Shail and Wilkinson, 1994; Shail and
131 Alexander, 1997). Tungsten deposits formed in cusped bodies of granite and their
132 immediately adjacent host rock (Hosking and Trounson, 1959; Jackson et al., 1989; Ball et
133 al., 1998). These deposits are commonly proximal to major NW-SE faults, e.g. Hemerdon,
134 Redmoor, Cligga Head (Figure 3), that have acted as strike-slip transfer faults during Early
135 Permian NW-SE extension, and appear to have influenced both magmatism and
136 mineralisation (Shail and Wilkinson, 1994; Shail et al., 2017).

137 1.1.2. Permian granite batholith

138 The Cornubian Batholith comprises five principal granite types: G1, two-mica granite; G2,
139 muscovite granite; G3, biotite granite; G4, tourmaline granite; G5, topaz granite (Simons et
140 al., 2016). The association between granite type and mineral prospectivity is not well-
141 constrained; granite types close to surface are sometimes older than, and unrelated to, the
142 mineralisation they host, e.g. Carnmenellis Granite (Moscati and Neymark, 2020).
143 Nevertheless, there is a strong association between W mineralisation and muscovite
144 granites (G2); these typically form small stocks and have been interpreted as a
145 differentiation product of two-mica (G1) granites, which also have an association with W
146 mineralisation (Simons et al., 2016, 2017). Tourmaline granites (G4) are common in areas of
147 significant tin mineralisation and have been interpreted as the precursor differentiated
148 magmas that released Sn-bearing magmatic-hydrothermal fluids (e.g. Müller et al., 2006).
149 Topaz granites (G5) host very low-grade disseminated Sn-W-Ta-Nb mineralisation and have
150 been inferred to be the source of substantial tourmalinisation haloes and associated Sn-W
151 mineralisation in the surrounding host rocks (Manning and Hill, 1990).

152 1.1.3. Tungsten mineralisation and exploration

153 Tungsten mineralisation in SW England, as reported in the British Geological Survey (BGS)
154 GeoIndex (2018), is shown in Figure 3. Additional tungsten occurrences are known, and
155 described in Dines (1956), but are not readily available in digital form and so were used
156 solely for qualitative evaluation.

157 Tungsten mineralisation is overwhelmingly hosted by sheeted veins and lodes. Wolframite is
158 the dominant ore mineral; scheelite is often present but usually minor (Jackson et al. 1989).
159 Sheeted veins typically comprise quartz ± tourmaline ± K-feldspar ± tourmaline-wolframite ±
160 cassiterite ± arsenopyrite and commonly display greisenized margins. They occur in well-
161 exposed stocks or dykes of muscovite (G2) granite, and their immediately adjacent host
162 rocks, and have been described in detail, e.g. Cligga Head (Hall, 1971; Moore and Jackson,

163 1977), St Michael's Mount (Dominy et al., 1995) and Hemerdon (Cameron, 1951; Dines,
164 1956; Shail et al., 2017). The Hemerdon deposit was recently operated by Wolf Minerals
165 Limited and produced tungsten and tin concentrates during 2015–2018. Lode
166 mineralisation usually occurs in two mica (G1) granites, e.g. Carnmenellis and Bodmin Moor,
167 and muscovite (G2) granites, and their immediately adjacent host rocks; assemblages can be
168 similar to those in sheeted veins, e.g. East Pool and Agar Mine and Castle-an-Dinas Mine
169 (Dines, 1956). However, wolframite also occurs in complex polymetallic lodes comprising
170 quartz ± tourmaline ± chlorite ± fluorite ± cassiterite ± arsenopyrite ± chalcopyrite ±
171 sphalerite, e.g. Roskear Complex Lode (Dines, 1956).

172 These magmatic-hydrothermal systems are Early Permian in age and synchronous with
173 batholith construction, based on Ar-Ar dating of muscovite wallrock alteration and U-Pb
174 dating of cassiterite (Chen et al. 1993; Chesley et al., 1993; Moscati and Neymark, 2020;
175 Tapster and Bright, 2020). Fluid inclusion studies, on vein quartz and cogenetic wolframite-
176 cassiterite, indicate typical magmatic-hydrothermal fluids temperatures in the range 300-
177 400°C (Jackson et al., 1977, 1989; Campbell and Panter, 1990; Smith et al., 1996). The
178 majority of vein and lode systems formed in response to Early Permian N-S regional
179 extension (Moore, 1975; Shail and Wilkinson, 1994) but coeval NW-SE transfer faults also
180 appear to have influenced magmatism and mineralisation (e.g. Shail and Wilkinson, 1994;
181 Shail et al., 2017).

182 Exploration has been selective and focused around known tungsten deposits. Andrews et al.
183 (1987) conducted soil geochemical studies around the Hemerdon deposit, which involved
184 three transects and identified geochemical anomalies, although no follow up trenching is
185 known. Geochemical exploration at Redmoor, which made use of an extensive diamond and
186 percussive drilling campaign as well as samples of float (rock fragments in soil), attempted
187 to define an alteration halo (Newall and Newall, 1989; Newall, 1994). The work used factor
188 analysis to identify a “mineralisation factor” for the elements As, Cu, W, Sn, Na* and Zr
189 (where * indicates a negative correlation). Beer et al. (1986) identified clear geochemical
190 anomalies for tungsten, based on percussive drilling along traverses, near to the Castle-an-
191 Dinas tungsten lode. The Mulberry and Wheal Prosper area was investigated by Bennett et
192 al. (1981) who found both tungsten and tin soil geochemical anomalies, in proximity to
193 Meadfoot Group calc-silicate units. Regional investigations were undertaken by Moore and
194 Camm (1982) and James and Moore (1985) using space-borne Landsat MSS and Seasat data
195 to map regional structures associated with tungsten mineralisation.

196 2. Data and Methods

197 The workflow illustrated in Figure 4 shows the steps required to incorporate knowledge-
198 based feature extraction into a data-driven modelling workflow to generate spatially refined
199 robust targets for mineral exploration. These include defining the conceptual deposit model,
200 initial data preparation (see Supplementary Information), feature extraction using fuzzy
201 transformations and machine learning modelling. It should be noted that, herein, the terms
202 *evidence layer* and *input variable* are used interchangeably.

203

204 2.1. Conceptual tungsten deposit model

205 The conceptual mineral deposit model enables the user to identify key exploration criteria.
206 These are represented by evidence layers, generated from available datasets. Regional
207 geological, geochemical and geophysical datasets have been incorporated in this work to
208 identify tungsten mineralisation in SW England. The contribution of these evidence layers to
209 the conceptual deposit model is described below.

210 Prior mineral exploration and geological investigations provide a substantial body of
211 research on which to build a regional conceptual tungsten deposit model for SW England
212 (Hosking and Trounson, 1959; Hall, 1971; Moore and Camm, 1982; Andrews et al., 1987;
213 Moore and Jackson, 1977; Jackson et al., 1989; Newall and Newall, 1989; Newall, 1994; Ball
214 et al., 1998, 2002; Shail et al., 2017). Based on these observations, a conceptual deposit
215 model has been developed to capture the common characteristics of known tungsten
216 deposits (Figure 5). The model is based on a range of readily available geological,
217 geochemical and geophysical datasets. Geological data comprises: (1) the mapped extent of
218 granite plutons based on British Geological Survey 1:50 000 data, and (2) a depth to granite
219 layer determined from the LiDAR Digital Terrain Model (DTM) and the granite surface
220 model, based on regional gravity data, created by Willis-Richards and Jackson (1989).
221 Geochemical datasets include soil and stream-sediment data from the G-BASE survey
222 (British Geological Survey, 2016), Tellus South West airborne geophysical surveys (Beamish
223 et al., 2014; Ferraccioli et al., 2014) and lineament data (Yeomans et al., 2019).

224 The evidence layers generated from these datasets have been prepared within the ESRI
225 ArcGIS Desktop software package. These data were resampled to a common extent and
226 resolution based on the airborne geophysical data (40 m pixels), and standardised to zero
227 mean and equal variance; as is usual in many machine learning approaches (Camps-Valls et
228 al., 2007; Hastie et al., 2009; Cracknell and Reading, 2015, 2014). The data preparation steps
229 for each layer are presented in the Supplementary Information (S1).

230 2.1.1. Geological evidence layers

231 The geological exploration criteria defined here are based on the observation that tungsten
232 mineralisation generally occurs, in granites or their host rocks, close to the margins of
233 “cusplate” granite bodies or cupolas, at the roof of the batholith (Hosking and Trounson,
234 1959; Beer et al., 1975; Dominy et al., 1995; Ball et al., 1998). An evidence layer for
235 proximity-to granite was prepared using the British Geological Survey 1:50 000 data to
236 capture the XY locations of granite contacts. A proximity-to granite layer was also prepared
237 to capture the depth to the granite contact in areas that may have blind mineralisation. The
238 granite surface from the 3D model created by Willis-Richards and Jackson (1989) is
239 subtracted from the LiDAR DTM and included as a proximity-to layer that captures the
240 proximity-to granite in Z (depth) to identify shallow granite bodies. Due to some areas of the
241 model protruding above surface, the evidence layer was classified into seven groups to
242 allow down-weighting of the protruding areas.

243 Structural information was also included, based on observations by Shail et al. (2017), using
244 regional lineament data derived from the airborne geophysics by Yeomans et al. (2019). A
245 proximity-to structures layer using a Euclidean distance algorithm was prepared based on
246 NW-SE lineaments with lengths > 1200 m; these lineaments are interpreted to be primarily

247 fault-controlled. Furthermore, a density map of all NW-SE lineaments was created to
248 capture areas of high fracturing that may favour mineralisation.

249 2.1.2. Geochemical evidence layers

250 Regional soil and stream-sediment geochemical data from the G-BASE survey (British
251 Geological Survey, 2016) were used to derive geochemical evidence layers. The soil samples
252 were collected at a depth of 0-20 cm and sieved to 2 mm. Stream-sediment samples were
253 analysed using X-ray Fluorescence Spectroscopy with no digestive reagent. Strict Quality
254 Assessment and Quality Control was conducted by the British Geological Survey prior to
255 release through the G-BASE survey; detailed by Wragg et al. (2018).

256 Geochemical evidence layers have been created through an Inverse-Distance Weighting
257 (IDW) algorithm based on preparation steps by Carranza (2010) and are summarised in
258 Table 1. Geochemical evidence layers are duplicated for both soil and stream-sediment
259 datasets discussed below, excluding the K/(Zr/Eu) layer. This ratio is exclusive to the stream-
260 sediment data due the absence of rare earth element analyses for soil samples. These data
261 are considered in three groups representing mineralisation, aureole and granite
262 geochemistry.

263 For mineralisation geochemistry, data on W as well as Sn, due to their common association,
264 is included (Cameron, 1951; Dines, 1956; Hall, 1971; Moore and Jackson, 1977; Jackson et
265 al., 1989). The use of As, Bi, Sb, Na*, Rb and Cs (where * indicates a negative correlation) is
266 based on the previous exploration campaigns.

267 As, Bi and Sb are used as indicators for mineralisation where tungsten and tin may be
268 unobserved. They occur at distance from the deposit (Andrews et al., 1987), therefore,
269 these elements may be a vector element in soil geochemistry for mineralisation at depth (or
270 laterally) where the main tungsten mineralisation is undercover and assuming there has
271 been minimal soil transport. Sb was considered to be an unreliable indicator element by Ball
272 et al. (2002) but is included in this study to determine its importance.

273 The inclusion of Na*, Rb and Cs and ratios such as K/Rb* and K/Cs* is based on aureole
274 geochemistry and alteration in mineralised country rocks surrounding granite cupolas
275 (Newall and Newall, 1989; Ball et al., 1998). Other elements that are enriched include Li and
276 F (Andrews et al., 1987; Newall and Newall, 1989; Newall, 1994; Ball et al., 1998), but there
277 are insufficient analyses for these elements across the region and they have therefore not
278 been included.

279 Litho-geochemical evidence layers are focused on granite types and these are defined using
280 two ratios. Ti/Sn* is useful for determining a general granite signature (Ball et al., 1984,
281 1998) but fails to separate granite types. By interrogating geochemical data from Simons et
282 al. (2016), an indicator ratio has been determined, K/(Zr/Eu), that separates the G2 granite
283 from other granite types (Figure 6), albeit with some close associations with the G1a type.
284 Other useful ratios have been identified, such as Zr/Fe₂O₃, Nb/Zr and Ba/Rb, but they are
285 not effective discriminators of G2 granites (Simons et al., 2016). Potential indicator elements
286 for G2 granite types include Be and Li (Simons et al., 2017); however, these are not included
287 in the available soil and stream-sediment geochemical datasets for the region.

288 2.1.3. Geophysical evidence layers

289 The geophysical evidence layers defined in the conceptual deposit model incorporate
290 airborne radiometric data from the Tellus South West project. The magmatic-hydrothermal
291 aureole around granite plutons in SW England is highlighted by $\tan^{-1}(K/eU^*)$. It is included
292 to capture hydrothermal alteration where elevated uranium concentrations indicate that
293 mineralising fluids may have circulated; as with geochemical ratios the evidence layer is an
294 inverse relationship. The inverse tangent function is applied to the ratio and results in a non-
295 linear normalisation with the data scaled from -1.57 to +1.57, which limits the effects of
296 outliers and potentially infinite values (Schetselaar, 2002; IAEA, 2003).

297 2.1.4. Training and validation data

298 A set of 34 known regional tungsten occurrences was compiled from the Mineral
299 Occurrence Database, maintained by the BGS GeolIndex (2018), and were used as true
300 positive samples. True negative samples are also necessary to accurately model and validate
301 unfavourable areas in the prospectivity models. An equal number of true negative samples
302 were randomly generated to ensure balanced training classes and minimise error rates
303 (Mellor et al., 2015). A minimum buffer of 400 m was applied to minimise spatial correlation
304 with true positive samples and other true negative samples. Furthermore, instead of one set
305 of true negative samples, 10 sets of 34 true negative samples generated as suggested by
306 Nykänen et al. (2017).

307 These sample sets were randomly subset 70:30 into 23 training and 11 validation data for
308 use in the fuzzy feature extraction methods discussed below. Multiple random sets of true
309 negative samples allow for testing of the random effect of point selection using the Receiver
310 Operating Characteristics (ROC) curve tool and the Area Under Curve (AUC) value (Nykänen
311 et al. 2017). By repeating the ROC curve analysis 10 times using randomly generated true
312 negative samples, Nykänen et al. (2017) demonstrated that a more robust metric is
313 obtained that highlights the potential for random variability in the AUC statistic.

314 For feature extraction, the training sample subsets are used to generate 10 ROC curve
315 analyses and determine the relevance and sensitivity of the evidence layer and tune the
316 parameters of the fuzzy transformation or combination.

317 For modelling, the 10 sets of 34 true negative samples were combined into a single dataset
318 and reselected randomly into new training and validation subsets using the same 70:30
319 split. The reselection of random points is aimed at reducing the likelihood of overfitting due
320 to feature extraction being honed by the same training data used for modelling. Model
321 training data used the true positive training subset and the first random true negative
322 training subset. The model testing (and final AUC values) used validation samples from all 10
323 reselected true negative validation subsets as part of the ROC curve analysis for model
324 evaluation.

325 2.2. Fuzzy feature extraction

326 The advent of high-resolution datasets of various types has meant that mineral prospectivity
327 models often include high numbers of input variables which increase the dimensionality.
328 Minimising the number of variables reduces data redundancy, which can improve

329 classification accuracy and reduce computation times (Witten et al., 2017). This process also
330 mitigates the “curse-of-dimensionality”, also known as the “Hughes effect” (Hughes, 1968),
331 whereby the number of training samples required to capture data variance increases
332 disproportionately with the number of variables. This is an important consideration when
333 only a small number of training samples is available. For these reasons, the extraction of the
334 most relevant features or characteristics within the evidence layers used in the prospectivity
335 modelling is of paramount importance.

336 A common and simple means of feature extraction is to use operators, such as
337 multiplication or division, to amplify the interactions between different variables (Henery,
338 1994a, 1994b). Some of these may also have the benefit of mitigating noise and removing
339 correlated data (Hastie et al., 2009); e.g. radioelement ratios (IAEA, 2003). Another option is
340 to highlight features using data transformations or image enhancements. There is a broad
341 range of task-specific transformations and enhancements that, when used with an
342 appropriate MLA, result in a high degree of accuracy (Sukumar et al., 2014).

343 In mineral prospectivity modelling, it is common to include ‘proximity-to’ evidence layers
344 which is an example of feature extraction, e.g. proximity-to structures. Many prospectivity
345 models attempt to refine the number of evidence layers using factor analysis, principal
346 component analysis or the singularity method to extract new features (Abedi et al., 2013;
347 Zhao et al., 2015; Wang et al., 2017a; Wang et al., 2017b; Wang et al., 2018). The Fuzzy
348 Logic approach incorporates the transformation and weighting of data and is also an
349 example of the feature extraction process where the fuzzy transformations and operators
350 enhance and accentuate particular characteristics.

351 The feature extraction methods discussed in this section concerns the reduction and
352 enhancement of the standardized variables generated during data preparation (see
353 Supplementary Information). This was conducted in ESRI ArcGIS software and the ArcSDM 5
354 package, maintained by the Geological Survey of Finland (GTK, 2019), which compiles
355 various tools for mineral prospectivity modelling. It includes the ROC curve tool that is used
356 to guide the subjective fuzzy data transformations.

357 2.2.1. The Receiver Operating Characteristics (ROC) curve tool

358 The output for mineral prospectivity modelling using MLAs is often a binary classification.
359 However, it is the class probabilities, the likelihood that a pixel is classified correctly, that
360 are of value when considering prospectivity (Harris et al., 2015). It is good practice to
361 evaluate the accuracy of the prospectivity models, most commonly through the ROC curve
362 tool (Agterberg and Bonham-Carter, 2005; Fawcett, 2006; Robinson and Larkins, 2007;
363 Nykänen, 2008). This uses *True Positives* (TP), *True Negatives* (TN), *False Positives* (FP) and
364 *False Negatives* (FN) to determine a range of metrics including *Sensitivity* (Equation 1) and
365 *Specificity* (Equation 2).

$$366 \quad \text{Sensitivity} = \frac{TP}{TP+FN} \quad (1)$$

$$367 \quad \text{Specificity} = \frac{TN}{TN+FP} \quad (2)$$

368 The ROC curve tool plots *Sensitivity* against $1 - \text{Specificity}$ and this can be used to calculate
369 the AUC. From a modelling perspective, the AUC values provide an accuracy measure with a

370 range between 0 and 1 where 0.5 represents a random result. During feature extraction,
371 more reliable features that capture the traits of true positive samples, are achieved by
372 maximising the AUC value by tuning the enhancement parameters. A minimised AUC value
373 is still useful in this instant as it represents a correlation with true negative samples and thus
374 has an inverse relationship to the model.

375 2.2.2. Fuzzy membership transformation

376 The subjective nature of fuzzy set theory and the Fuzzy Logic method can be circumvented
377 by refining input variables using the ROC curve tool developed by Nykänen et al. (2015,
378 2017). The approach provides a quantitative metric for assessing subjective aspects of the
379 Fuzzy Logic technique, namely the application of the fuzzy membership function and fuzzy
380 operators such as *FuzzyOR* (An et al., 1991; Bonham-Carter, 1994). The tool optimises the
381 output of these functions and operators and allows tuning of the features to reflect the
382 characteristics of known deposits. In turn, the correlation of an input layer can be used to
383 indicate whether it is correctly included as part of the conceptual deposit model.

384 The method applied here used an iterative approach to assess the fuzzy membership
385 function where initial evidence layers are transformed by determining a *spread* and
386 *midpoint*. Once a variable was determined to be ascending or descending, e.g. the target
387 values are small or large, respectively, the *spread* and *midpoint* were tuned to create a layer
388 with the best AUC value with associated mean, median and standard deviation. This
389 approach provides information on the variability caused by random points and of feature
390 sensitivity, whilst minimising the chance of a biased true negative sample set affecting the
391 transformation. Note that the Proximity-to Granite in Z layer was generated using the Table
392 of Contents (TOC) function from the ArcSDM 5 package.

393 A list of the final input variables and the optimised parameters used for the fuzzy
394 membership functions is provided in Table 2; full results for all tested parameters are
395 presented in the Supplementary Information (S1). It is clear that some input variables have a
396 much higher AUC than others. Nykänen et al. (2017) suggest there is value in the inclusion
397 of a variable even where AUC values are close to 0.5 (random correlation) because it may
398 provide mutually beneficial information to a subsequent combination of variables later in
399 the analysis.

400 2.2.3. Fuzzy operator combinations

401 Following fuzzy membership transformation, some associated input variables were
402 combined into single layers to not only enhance the feature, but to also assist with
403 dimensionality reduction. Elements with geochemical analyses in the form of both soil and
404 stream-sediment data were integrated into single variables to represent the overall
405 anomalies for that element (Figure 7). The same approach was also applied to geochemical
406 ratios, with the exception of K/(Zr/Eu), as this was only created for stream-sediment data
407 due to the absence of soil REE analyses for the soil data. A visual inspection of the data was
408 conducted prior to integration to ensure that the values for each variable were comparable.

409 The *fuzzyOR* operator is considered to be the best tool to combine two elements or ratios
410 into a single input variable to maximise potential anomalies (Bonham-Carter, 1994), as well
411 as reduce dimensionality in the model, and it is used here to maximise indications of

412 geochemical anomalies from both datasets. These were subsequently reassessed using the
413 ROC curve tool and new AUC values were calculated (Table 3). For W, Sn, As and Na, this
414 results in a synergistic effect where the AUC is greater than both AUC values for the
415 individual datasets. For Bi, Sb, Rb, Cs, K/Cs, K/Rb and Ti/Sn, the AUC values fall between the
416 lower and upper values derived for the original datasets.

417 2.3. Machine learning for prospectivity modelling

418 Various MLAs are available for prospectivity modelling, however, it is the Random Forest
419 algorithm that has consistently proven to be highly effective in comparison to Support
420 Vector Machines and Artificial Neural Networks (Carranza and Laborde, 2015a, 2015b;
421 Rodriguez-Galiano et al., 2015; Carranza and Laborde, 2016; Sun et al., 2019). For this
422 reason, two Random Forest models are presented for prospectivity modelling, using: (i)
423 standardized input variables with no transformation; (ii) variables transformed using the
424 guided fuzzy set theory approach of Nykänen et al. (2015, 2017).

425 An advantage of using MLAs for mineral prospectivity modelling is the evaluation metrics
426 available for each algorithm. Many classification methods allow the probability of a pixel
427 being correctly classified, the class probabilities, to be interrogated. For mineral
428 prospectivity modelling, class probabilities are often presented as the final result, but these
429 can be further manipulated through model variance (Kohavi and Wolpert, 1996; Cracknell
430 and Reading, 2013). Model variance was implemented as part of lithological mapping by
431 Cracknell and Reading (2013) in the Broken Hill area of New South Wales, Australia where
432 higher variance was an indicator for the presence of fault zones and was termed “the upside
433 of uncertainty”. This was further investigated using information entropy (Kuhn et al., 2018).

434 There is often a predilection for distilling model performance to a single accuracy metric.
435 However, this is not ideal, especially with spatial data where some aspects of the model may
436 be well-constrained and other components highly suspect. By incorporating a spatial
437 assessment of model reliability into the evaluation process, the user can enhance the
438 analysis and mitigate the potential limitations of a single accuracy metric. To this end, we
439 develop a new Confidence Metric, founded on model variance, to evaluate the model and
440 further investigate the extent of prospective areas before giving some quantification of the
441 depth to potential targets.

442 2.3.1. Random Forest modelling

443 Prospectivity modelling was performed using the *R* statistical computing language (R Core
444 Team, 2019). A binary MLA classification model was created where two classes were used
445 (unfavourable and favourable) to determine a simple class probability model. The Random
446 Forest models were implemented using the *caret* (Kuhn et al., 2019), *raster* (Hijmans, 2019)
447 and *rgdal* (Bivand et al., 2019) packages. A full description of the *R* workflow is presented in
448 the Supplementary Information (S2).

449 The Random Forest method is an ensemble decision tree machine learning algorithm first
450 described by Breiman (2001). The method has become increasingly popular in geoscience
451 and has been used in prospectivity modelling for a range of ore deposit types (e.g. O’Brien
452 et al., 2014; Harris et al., 2015; Carranza & Laborde 2015a, 2015b, 2016; Gao et al., 2017;
453 Hariharan et al., 2017; Li et al., 2019; Sun et al., 2019). The approach combines multiple

454 binary-split trees which limits overfitting that can occur through multi-split trees (Hastie et
 455 al., 2009). The Random Forest algorithm, illustrated in Figure 8, utilises multiple decision
 456 trees (the forest) which attempt to split a random selection of input variables. The number
 457 of random variables is controlled by the user-defined *mtry* value that can be determined
 458 using a random or grid search to find the best value, or, as in this study, by calculating the
 459 square root of the number of input variables (Breiman, 2001; Gislason et al., 2006; Belgiu
 460 and Drăguț, 2016). A further parameter must be set, *ntree*, which dictates the number of
 461 binary trees in the forest and controls the reproducibility of the results. Based on a review
 462 by Belgiu and Drăguț (2016), *ntree* is commonly set to 500 for most classification problems
 463 using remote sensing data. Carranza and Laborte (2015b) increased *ntree* to 20 000 in order
 464 to achieve stable predictions and lower the prediction error for a training set of 12 samples.
 465 Given the comparably small training sample size in this study (23 training samples and 11
 466 validation samples), the *ntree* value of 20 000 was also adopted here.

467 A total of 28 input variables are included in the standardised model (see Table 2), while 17
 468 variables are included in the fuzzy-transformed model following combination of duplicate
 469 geochemical elements using the *fuzzyOR* operator (see Table 3). All fuzzy-transformed and
 470 combined data were included in the modelling process despite the potentially low relevance
 471 of Sb. The inclusion of Sb is due to its minor positive correlation with known deposits that
 472 may still contribute some relevant information.

473 The models were evaluated using the ROC curve tool to derive the mean and median AUC
 474 values and associated standard deviation for each model using the true positive validation
 475 subset and the 10 randomly reselected true negative validation subsets (described in
 476 Section 2.1.4).

477 2.3.2. The Confidence Metric

478 Spatial evaluation of the model can be undertaken by calculating the model variance
 479 (Equation 3) of the class probabilities to derive an uncertainty value (Kohavi and Wolpert,
 480 1996). This approach was implemented by Cracknell and Reading (2013) to show areas
 481 where the classification is less reliable. In this study, model variance is exploited to
 482 determine whether favourable targets are truly robust in the mineral prospectivity model.
 483 By combining model variance and the class probabilities into the new Confidence Metric
 484 using Equation 4, exploration targets can be refined to highlight the areas of highest
 485 confidence in the model.

$$486 \quad \text{model variance } (v) = \frac{1 - \sum p_c^2}{1 - \sum (\frac{1}{c})} \quad (3)$$

487 Where p_c is the class probability for each class per pixel and c is the total number of classes.

$$488 \quad \text{confidence } (p_{conf}) = \frac{(p_c - v)_i - \min(p_c - v)}{\max(p_c - v) - \min(p_c - v)} \quad (4)$$

489
 490 Where i indicates a per pixel subtraction.

491 By subtracting the model variance, the values of pixels with high uncertainty are reduced
 492 accordingly, leaving only the most reliable areas with high class probabilities. In some cases,

493 this can reduce the value to less than zero and, for the purposes of comparison, Equation 4
494 normalises the output to a range of 0 to 1.

495 2.3.3. Areal evaluation

496 The spatial distribution of the prospectivity is quantitatively evaluated using areal analysis.
497 Total areal extents are calculated for each level of prospectivity, unfavourable through to
498 highly favourable, as a sum of the area for each level and as a percentage of total area of
499 the model. The analysis provides a quantitative assessment of the spatial distribution of the
500 class probabilities for each model and the associated confidence. The proportion of pixels at
501 each prospectivity level are compared to determine which model is better at discriminating
502 prospective areas.

503 2.3.4. Depth evaluation

504 The rich mining history of SW England means that there is an extensive repository of data
505 but the quality of digital records is highly variable. Legacy mining data is available through
506 the British Geological Survey from the Mineral Exploration and Investigation Grants Act
507 (MEIGA) records and published works such as Dines (1956). These resources are used to
508 further evaluate the depth at which potential targets may occur.

509 3. Results and Discussion

510 The results of the MLA modelling using both feature extraction methods are presented
511 below. These are assessed, based on the AUC values from ROC curve analysis, and further
512 evaluated using the Confidence Metric, areal analysis and legacy mining data. These
513 evaluation techniques aim, respectively, to generate robust targets, compare the spatial
514 attributes of the model and to give an indication of whether targets are likely to reside at
515 surface or at depth.

516 3.1. Tungsten prospectivity modelling results

517 The results of the modelling using standard and fuzzy input variables are presented in Figure
518 9 and Figure 10. Each figure comprises the binary classification of all prospective areas, the
519 class probability for a cell being classified as prospective and the confidence map derived
520 using the Equation 4.

521 The class map for the prospectivity model shows broad areas of prospective areas for
522 tungsten mineralisation due to the binary classification. The Random Forest class probability
523 map is therefore more useful as it signifies the likelihood that a location is prospective. For
524 Figure 9 and Figure 10, the data have been categorised to show only values greater than 0.5
525 in colour, this is to indicate that anything below this value would have been classified as
526 unfavourable in the binary classification.

527 The class probability map for the standardised variables (Figure 9) shows a good correlation
528 with known tungsten occurrences. Areas of high favourability are constrained to areas of
529 known deposits marked as W-Y in Figure 9b, which include the Camborne-Redruth district,
530 the St Austell district and the east Bodmin-Kit Hill area, respectively. However, no highly

531 favourable areas are identified that were not previously known and only limited areas have
532 been identified as favourable.

533 Figure 10 shows the class probability map for the fuzzy-transformed variables that identifies
534 highly favourable areas over known tungsten occurrences, similar to those in Figure 9b (W-
535 Y), including the Cligga Head area (Z). Additional areas include the Breage district (A), the
536 southern margin of the Bodmin Granite (B) and some discrete targets along the eastern
537 margin of the Dartmoor Granite (C) which are new prospects. The map also shows broader
538 areas of favourable prospectivity away from main targets.

539 The ROC curve tool was used to validate these models and generate a quantitative measure
540 of accuracy for the binary classification. A summary of the validation results from the ROC
541 curve analysis is included in Table 4. The average AUC values for both class probability
542 models are very high and not significantly different. It is unsurprising that both models have
543 such similar AUC values due to sharing the same initial evidence layers and the invariance of
544 the Random Forest algorithm to changes in scale (but not *midpoint* and *spread*) imparted by
545 the fuzzy membership transformation. Furthermore, the similarity in AUC values underlines
546 that the use of training samples with the ROC curve tool during feature extraction has not
547 overly biased the model. However, the reduction in dimensionality from 28 to 17 input
548 variables in the fuzzy-transformed model appears to have provided no significant
549 improvements to the modelling process.

550 Despite the minimal difference in AUC values, the lack of new highly prospective targets in
551 the standardised variable model is disappointing. Nevertheless, the greater number of new
552 targets in the fuzzy-transformed model indicates that the incorporation of user-knowledge,
553 through fuzzy-transformed variables during feature extraction, has refined target
554 identification within a data-driven Random Forest modelling approach.

555 3.2. Target confidence

556 The use of model variance (Equation 3) and manipulation of this metric into a measure of
557 target confidence is novel and has demonstrated significant value for evaluating the
558 prospectivity models. The confidence maps for each model shown in Figure 9c and Figure
559 10c reveal highly favourable and favourable areas that are not only significantly refined in
560 area, but define more reliable targets. Any area shown to be >0.5 in terms of confidence
561 should be compared to the class probability map to determine its favourability and those
562 areas with high class probabilities and high confidence are likely to be robust. Therefore, the
563 confidence map helps to elucidate highly favourable and favourable areas and interpret
564 reliable exploration targets. Furthermore, it gives a greater understanding where the model
565 has performed best and goes beyond the use of single accuracy metrics which can be
566 misleading.

567 3.3. Model comparison from areal evaluation

568 The two Random Forest models presented here can also be assessed to determine the
569 prospectivity by area. Models for class probability and confidence have been assessed in
570 terms of area in Table 5. These show the total area and normalised area for each class
571 shown in Figure 9 and Figure 10.

572 The total areas are similar for each model and small discrepancies are due to rounding
573 errors. The class probability model for standardised variables shows a greater proportion of
574 the study area having some degree of prospectivity (>0.5). In contrast, the class probability
575 model for the fuzzy-transformed variables shows a smaller proportion of the study area to
576 be prospective (>0.5) but the areas that are identified have a greater degree of
577 prospectivity. The most prospective areas (>0.8) accounts for 3.7% of the total area
578 compared to 2% when using standardised variables. Similarly, the confidence model for
579 both methods has been assessed. If a value of >0.5 is taken as a reasonable confidence level,
580 3.2% and 5.2% of the models for standard variables and fuzzy-transformed variables,
581 respectively, can be considered to be robust.

582 The results from this analysis would infer that the fuzzy-transformed variables give an
583 overall greater confidence when generating exploration targets compared to the
584 standardised variables. By revisiting Table 3, it can be seen that the combination of W, Sn,
585 As and Na has a mutually beneficial effect on the AUC values compared to the prior values
586 for the individual soil and stream-sediment geochemical layers. These mutually beneficial
587 combinations are likely to improve the MLA model and enhance target delineation.

588 3.4. Evaluation using legacy mining data

589 New targets were identified from the Random Forest model using fuzzy-transformed
590 variables. These include the Breage district, the southern margin of the Bodmin Granite and
591 a series of discrete targets along the eastern margin of the Dartmoor Granite labelled A, B
592 and C, respectively (Figure 10b). These are further highlighted in Figure 11 alongside
593 additional legacy data to further assess the fuzzy-transformed variable model.

594 In the Breage district (Figure 11a), historic mining records indicate tungsten mineralisation
595 was intersected at depth at Prospidnick on the SW margin of the Carnmenellis Granite and
596 at Great Wheal Fortune on the eastern margin of the Tregonning-Godolphin Granite (Dines,
597 1956). Furthermore, a borehole was drilled in the area to 214.14 m that intersected the
598 granite contact at 173.6 m where the upper 20 m showed greisen textures and reported
599 tungsten and tin mineralization in assay (Ball et al., 1984). Note, this occurrence is missing
600 from the BGS GeoIndex (2018) data.

601 Studies conducted under MEIGA are not recorded in the BGS GeoIndex (2018). The
602 mineralisation along the southern margin of the Bodmin Granite (Figure 11b) was
603 investigated by Consolidated Gold Fields Ltd as part of regional tungsten exploration study
604 funded by MEIGA in 1972. Tungsten and tin anomalies were identified in streams and
605 follow-up soil sampling was also conducted. A drilling campaign along the southern margin
606 of the granite was conducted which intersected tungsten mineralisation but grades and
607 tonnages were deemed uneconomic at the time.

608 Targets identified in Figure 11c along the eastern margin of the Dartmoor Granite require
609 further follow-up work. No records of tungsten have been found, however, four mines are
610 inferred by Dines (1956) to become uneconomic with depth with respect to tin and it was
611 suggested that other “uneconomic” metals may exist but are not described further. One of
612 these mines exists outside of the surface crop of the granite and intersects the granite
613 margin at approximately 90 m below surface.

614 The use of these additional resources helps validate the mineral prospectivity model. The
615 reference to tungsten mineralisation found in old mines and former drilling projects
616 suggests that some of these targets may be within a few hundred metres of surface. This
617 further supports the model for identifying blind deposits and the inclusion of the proximity-
618 to granite in Z evidence layer is likely to be important; high resolution gravity measurements
619 may improve the analysis significantly.

620 Conclusions

621 Mineral prospectivity modelling has been conducted using a data-driven Random Forest
622 MLA approach for tungsten in SW England. A particular focus has been put on feature
623 extraction and the use of initial variables that were standardised to zero mean and equal
624 variance compared to those that were further processed using knowledge-driven fuzzy
625 membership and fuzzy overlay functions.

626 The two models presented here have similar accuracies based on ROC curve analysis but
627 show different spatial distributions of prospectivity in the region. The model that uses
628 standardised variables only identifies areas of high prospectivity (>0.9) proximal to the
629 training data. The second model, using fuzzy-transformed input variables, identifies three
630 new highly prospective targets that were previously unidentified in the training data. The
631 improvement in target generation is directly attributable to the use of knowledge-driven
632 feature extraction techniques within a data-driven MLA framework.

633 These models are enhanced using model variance to derive a new Confidence Metric. The
634 Confidence Metric is a simple calculation to infer where class probabilities are most robust.
635 These are presented as a map that can be combined with the initial class probabilities to
636 determine the most reliable targets. The approach results in spatially refined and robust
637 mineral exploration targets that can allow for a more focussed follow-up field campaign.

638 The models have been further evaluated by an areal analysis showing that the fuzzy-
639 transformed model is a better discriminator for prospective areas compared to the
640 standardised variable model due to the mutually beneficial effect of combining geochemical
641 layers such as W, Sn, As and Na during feature extraction. Also, the fuzzy-transformed
642 model has greater confidence and generates a greater proportion of robust targets by area
643 based on the Confidence Metric. By conducting model evaluation in this way, two models
644 with the same statistical accuracy but different spatial distributions can be better
645 understood. This study underlines how single accuracy metrics can be fallible when applied
646 to spatial datasets.

647 Finally, the use of legacy mining data further reinforces the strength of the model where all
648 three new target areas have potential economic mineralisation either through direct
649 sampling or inferred from mine descriptions. Further, the legacy mining data suggests that
650 the targets generated may be within 300 m of surface. This would indicate the "Proximity-to
651 granite in Z" evidence layer derived from regional gravity data is valuable and that new
652 discoveries of tungsten mineralisation in SW England may be enhanced by a new high-
653 resolution gravity survey.

654 Acknowledgements

655 We thank two anonymous reviewers for their comments that improved the final
656 manuscript. CMY would like to thank Dr Charles Moon for his comments on an early draft
657 and Dr Anya Reading for constructive conversations during CMY's viva voce examination.
658 The work was completed as part of doctoral research by CMY funded by the British
659 Geological Survey (S267) and the Natural Environment Research Council (NERC) GW4+
660 Doctoral Training Partnership (NE/L002434/1) in collaboration with the Geological Survey of
661 Finland (GTK). Data used in this study are available from the Tellus South West project
662 website (www.tellusgb.ac.uk). PL publishes with the permission of the Executive Director,
663 British Geological Survey (UKRI).

664 References

- 665 Abedi, M., Norouzi, G.H., Torabi, S.A., 2013. Clustering of mineral prospectivity area as an
666 unsupervised classification approach to explore copper deposit. *Arabian Journal of*
667 *Geosciences* 6, 3601–3613. <https://doi.org/10.1007/s12517-012-0615-5>
- 668 Agterberg, F.P., Bonham-Carter, G.F., 2005. Measuring the performance of mineral-potential
669 maps. *Natural Resources Research* 14, 1–17. <https://doi.org/10.1007/s11053-005-4674-0>
- 670 Alexander, A.C., Shail, R.K., 1996. Late- to post-Variscan structures on the coast between
671 Penzance and Pentewan, South Cornwall. *Proceedings of the Ussher Society* 9, 72–78.
- 672 Alexander, A.C., Shail, R.K., 1995. Late Variscan structures on the coast between
673 Perranporth and St. Ives, Cornwall. *Proceedings of the Ussher Society* 8, 398–404.
- 674 An, P., Moon, W.M., Rencz, A., 1991. Application of fuzzy set theory to integrated mineral
675 exploration. *Canadian Journal of Exploration* 27, 1–11. <https://doi.org/10.3997/2214-4609.201410970>
- 677 Andrews, M.J., Ball, T.K., Fuge, R., Nicholson, R.A., Peachey, D., 1987. Trace elements in soils
678 around the Hemerdon tungsten deposit, Devon; implications for exploration. *Proceedings of*
679 *the Ussher Society* 6, 536–541.
- 680 Bahiru, E.A., Woldai, T., 2016. Integrated geological mapping approach and gold
681 mineralization in Buhweju area, Uganda. *Ore Geology Reviews* 72, 777–793.
682 <https://doi.org/10.1016/j.oregeorev.2015.09.010>
- 683 Ball, T.K., Basham, I.R., Charoy, B., 1984. Petrogenesis of the Bosworgey granitic cusp in the
684 SW England tin province and its implications for ore mineral genesis. *Mineralium Deposita*
685 19, 70–77. <https://doi.org/10.1007/BF00206599>
- 686 Ball, T.K., Fortey, N.J., Beer, K.E., 2002. Aspects of the lithogeochemistry of arsenic,
687 antimony and bismuth in South West England. *Geoscience in South-West England* 10, 352–
688 357.
- 689 Ball, T.K., Fortey, N.J., Beer, K.E., 1998. Alkali metasomatism from Cornubian granite
690 cupolas. *Geoscience in South-West England* 9, 171–177.

691 Beamish, D., Howard, A., Ward, E.K., White, J., Young, M.E., 2014. Tellus South West
692 airborne geophysical data.

693 Beer, K.E., Ball, T.K., Bennett, M.J., 1986. Mineral investigations near Bodmin, Cornwall. Part
694 5 - The Castle-an-Dinas wolfram lode. Mineral Reconnaissance Programme Report, British
695 Geological Survey. No.82; Mineral Reconnaissance Programme Report, British Geological
696 Survey. No.82.

697 Beer, K.E., Burley, A.J., Tombs, J.M., 1975. The concealed granite roof in south-west
698 Cornwall. Mineral Reconnaissance Programme Report, Institute of Geological Sciences, No.1
699 [Unpublished]; Mineral Reconnaissance Programme Report, Institute of Geological Sciences,
700 No.1 [Unpublished].

701 Belgiu, M., Drăguț, L., 2016. Random forest in remote sensing: A review of applications and
702 future directions. *ISPRS Journal of Photogrammetry and Remote Sensing* 114, 24–31.
703 <https://doi.org/10.1016/j.isprsjprs.2016.01.011>

704 Bennett, M.J., Beer, K.E., Jones, R.C., Turton, K., Rollin, K.E., Tombs, J.M.C., Patrick, D.J.,
705 1981. Mineral investigations near Bodmin, Cornwall. Part 3 - The Mulberry and Wheal
706 Prosper area. Mineral Reconnaissance Programme Report. Institute of Geological Sciences,
707 No. 48; Mineral Reconnaissance Programme Report. Institute of Geological Sciences, No. 48.

708 BGS GeoIndex, 2018. Mineral Occurrence
709 Database. <https://www.bgs.ac.uk/mineralsuk/data/mineocc.html>

710 Bivand, R., Keitt, T., Rowlingson, B., 2019. rgdal: Bindings for the 'Geospatial' Data
711 Abstraction Library. <https://cran.r-project.org/package=rgdal>

712 Bonham-Carter, G.F., 1994. Geographic information systems for geoscientists: modelling
713 with GIS, First. ed. Elsevier Science Ltd, Kidlington, UK.

714 Breiman, L., 2001. Random forests. *Machine Learning* 45, 5–32.
715 <https://doi.org/10.1023/A:1010933404324>

716 British Geological Survey, 2016. G-BASE for Southwest England.

717 Cameron, J., 1951. The Geology of the Hemerdon wolfram mine, Devon. *Transactions of the*
718 *Institution of Mining and Metallurgy* 6L, 1–14.

719 Campbell, A.R. and Panter, K.S., 1990. Comparison of fluid inclusions in coexisting
720 (cogenetic?) wolframite, cassiterite, and quartz from St. Michael's Mount and Cligga Head,
721 Cornwall, England. *Geochimica et Cosmochimica Acta*, 54, 673-681

722 Camps-Valls, G., Bandos Marsheva, T.V., Zhou, D., 2007. Semi-supervised graph-based
723 hyperspectral image classification. *IEEE Transactions on Geoscience and Remote Sensing* 45,
724 3044–3054. <https://doi.org/10.1109/TGRS.2007.895416>

725 Carranza, E. J. M. (2009). Objective selection of suitable unit cell size in data-driven
726 modeling of mineral prospectivity. *Computers and Geosciences*, 35(10), 2032–2046.
727 <https://doi.org/10.1016/j.cageo.2009.02.008>

728 Carranza, E.J.M., 2010. Mapping of anomalies in continuous and discrete fields of stream
729 sediment geochemical landscapes. *Geochemistry: Exploration, Environment, Analysis* 10,
730 171–187. <https://doi.org/10.1144/1467-7873/09-223>

731 Carranza, E.J.M., Laborte, A.G., 2016. Data-Driven Predictive Modeling of Mineral
732 Prospectivity Using Random Forests: A Case Study in Catanduanes Island (Philippines).
733 *Natural Resources Research* 25, 35–50. <https://doi.org/10.1007/s11053-015-9268-x>

734 Carranza, E.J.M., Laborte, A.G., 2015a. Data-driven predictive mapping of gold prospectivity,
735 Baguio district, Philippines: Application of Random Forests algorithm. *Ore Geology Reviews*
736 71, 777–787. <https://doi.org/10.1016/j.oregeorev.2014.08.010>

737 Carranza, E.J.M., Laborte, A.G., 2015b. Random forest predictive modeling of mineral
738 prospectivity with small number of prospects and data with missing values in Abra
739 (Philippines). *Computers and Geosciences* 74, 60–70.
740 <https://doi.org/10.1016/j.cageo.2014.10.004>

741 Chen, Y., Clark, A. H., Farrar, E., Wasteneys, H. A. H. P., Hodgson, M. J., & Bromley, A. V.
742 (1993). Diachronous and independent histories of plutonism and mineralization in the
743 Cornubian Batholith, southwest England. *Journal of the Geological Society, London*, 150,
744 1183–1191

745 Coward, M.P., Smallwood, S., 1984. An interpretation of the Variscan tectonics of SW
746 Britain. *Geological Society, London, Special Publications* 14, 89–102.
747 <https://doi.org/10.1144/GSL.SP.1984.014.01.08>

748 Cracknell, M.J., Reading, A.M., 2015. Spatial-Contextual Supervised Classifiers Explored: A
749 Challenging Example of Lithostratigraphy Classification. *IEEE Journal of Selected Topics in*
750 *Applied Earth Observations and Remote Sensing* 8, 1371–1384.
751 <https://doi.org/10.1109/JSTARS.2014.2382760>

752 Cracknell, M.J., Reading, A.M., 2014. Geological mapping using remote sensing data: A
753 comparison of five machine learning algorithms, their response to variations in the spatial
754 distribution of training data and the use of explicit spatial information. *Computers and*
755 *Geosciences* 63, 22–33. <https://doi.org/10.1016/j.cageo.2013.10.008>

756 Cracknell, M.J., Reading, A.M., 2013. The upside of uncertainty: Identification of lithology
757 contact zones from airborne geophysics and satellite data using random forests and support
758 vector machines. *Geophysics* 78, 113–126. <https://doi.org/10.1190/GEO2012-0411.1>

759 Dearman, W.R., 1970. Some aspects of the tectonic evolution of South-West England.
760 *Proceedings of the Geologists' Association* 81, 483–491. [https://doi.org/10.1016/S0016-](https://doi.org/10.1016/S0016-7878(70)80009-8)
761 [7878\(70\)80009-8](https://doi.org/10.1016/S0016-7878(70)80009-8)

762 Dearman, W.R., 1963. Wrench-faulting in Cornwall and south Devon. *Proceedings of the*
763 *Geologists' Association* 74, 265–287. [https://doi.org/10.1016/S0016-7878\(63\)80023-1](https://doi.org/10.1016/S0016-7878(63)80023-1)

764 Dines, H.G., 1956. The Metalliferous mining region of south-west England. *Economic*
765 *Memoirs of the Geological Survey of Great Britain*.

766 Dominy, S.C., Camm, G.S., Bussell, M.A., Scrivener, R.C., Halls, C., 1995. A review of tin
767 stockwork mineralization in the south-west England orefield. *Proceedings of the Ussher*
768 *Society* 8, 368–373.

769 Fawcett, T., 2006. An introduction to ROC analysis. *Pattern Recognition Letters* 27, 861–874.
770 <https://doi.org/10.1016/j.patrec.2005.10.010>

771 Ferraccioli, F., Gerard, F., Robinson, C., Jordan, T., Biszczuk, M., Ireland, L., Beasley, M.,
772 Vidamour, A., Barker, A., Arnold, R., Dinn, M., Fox, A., Howard, A., 2014. LiDAR based Digital
773 Terrain Model (DTM) data for South West England. [https://doi.org/10.5285/e2a742df-3772-](https://doi.org/10.5285/e2a742df-3772-481a-97d6-0de5133f4812)
774 [481a-97d6-0de5133f4812](https://doi.org/10.5285/e2a742df-3772-481a-97d6-0de5133f4812)

775 Gao, Y., Zhang, Z., Xiong, Y., & Zuo, R. (2016). Mapping mineral prospectivity for Cu
776 polymetallic mineralization in southwest Fujian Province, China. *Ore Geology Reviews*, 75,
777 16–28. <https://doi.org/10.1016/j.oregeorev.2015.12.005>

778 Gislason, P.O., Benediktsson, J.A., Sveinsson, J.R., 2006. Random forests for land cover
779 classification. *Pattern Recognition Letters* 27, 294–300.
780 <https://doi.org/10.1016/j.patrec.2005.08.011>

781 GTK, 2019. ArcSDM. <https://github.com/gtkfi/ArcSDM>

782 Hall, A., 1971. Greisenisation in the granite of Cligga Head, Cornwall. *Proceedings of the*
783 *Geologists' Association* 82, 209–230.

784 Hariharan, S., Tirodkar, S., Porwal, A., Bhattacharya, A., & Joly, A. (2017). Random Forest-
785 Based Prospectivity Modelling of Greenfield Terrains Using Sparse Deposit Data: An Example
786 from the Tanami Region, Western Australia. *Natural Resources Research*, 26(4), 489–507.
787 <https://doi.org/10.1007/s11053-017-9335-6>

788 Harris, J.R., Grunsky, E., Behnia, P., Corrigan, D., 2015. Data- and knowledge-driven mineral
789 prospectivity maps for Canada's North. *Ore Geology Reviews* 71, 788–803.

790 Hastie, T., Tibshirani, R., Friedman, J., 2009. *The Elements of Statistical Learning*, Springer
791 series in statistics. Springer New York, New York, NY. [https://doi.org/10.1007/978-0-387-](https://doi.org/10.1007/978-0-387-84858-7)
792 [84858-7](https://doi.org/10.1007/978-0-387-84858-7)

793 Henery, R.J., 1994a. Classification, in: Michie, D., Spiegelhalter, D.J., Taylor, C.C. (Eds.),
794 *Machine Learning, Neural and Statistical Classification*. Ellis Horwood, New York, pp. 6–16.

795 Henery, R.J., 1994b. Methods for Comparison, in: Michie, D., Spiegelhalter, D.J., Taylor, C.C.
796 (Eds.), *Machine Learning, Neural and Statistical Classification*. Ellis Horwood, New York, pp.
797 107–124.

798 Hijmans, R.J., 2019. raster: Geographic Data Analysis and Modeling. [https://cran.r-](https://cran.r-project.org/package=raster)
799 [project.org/package=raster](https://cran.r-project.org/package=raster)

800 Hobson, D.M., Sanderson, D.J., 1983. Variscan Deformation in Southwest England, in:
801 Hancock, P.L. (Ed.), *The Variscan Fold Belt in the British Isles*. Adam Hilger Ltd, Bristol, pp.
802 108–129.

803 Hosking, K.F.G., Trounson, J.H., 1959. The mineral potential of Cornwall, in: Non-Ferrous
804 Mining in Great Britain and Ireland. Institution of Mining; Metallurgy Symposium, London,
805 pp. 335–369.

806 Hughes, G.F., 1968. On the Mean Accuracy of Statistical Pattern Recognizers. IEEE
807 Transactions on Information Theory 14, 55–63. <https://doi.org/10.1109/TIT.1968.1054102>

808 IAEA, 2003. Guidelines for radioelement mapping using gamma ray spectrometry data,
809 IAEA-TECDOC-1363. International Atomic Energy Agency, Vienna, Austria.

810 Jackson, N.J., Willis-Richards, J., Manning, D.A.C., Sams, M.S., 1989. Evolution of the
811 Cornubian ore field, Southwest England; Part II, Mineral deposits and ore-forming
812 processes. *Economic Geology* 84, 1101–1133.

813 James, J.M., Moore, J.M., 1985. Multi-seasonal imagery studies for geological mapping and
814 prospecting in cultivated terrain of S.W. England, in: Fourth Thematic Conference: "Remote
815 Sensing for Exploration Geology", San Francisco, California, April 1-4, 1985. San Francisco,
816 California, pp. 475–484.

817 Kohavi, R., Wolpert, D.H., 1996. Bias plus variance decomposition for zero-one loss
818 functions, in: Proceedings of the 13th International Conference on Machine Learning
819 (Icml96), Bari, Italy. pp. 275–283.

820 Kreuzer, O.P., Markwitz, V., Porwal, A.K., McCuaig, T.C., 2010. A continent-wide study of
821 Australia's uranium potential. Part I: GIS-assisted manual prospectivity analysis. *Ore Geology
822 Reviews* 38, 334–366. <https://doi.org/10.1016/j.oregeorev.2010.08.003>

823 Kuhn, M., Wing, J., Weston, S., Williams, A., Keefer, C., Engelhardt, A., Cooper, T., Mayer, Z.,
824 Kenkel, B., the R Core Team, Benesty, M., Lescarbeau, R., Ziem, A., Scrucca, L., Tang, Y.,
825 Candan, C., Hunt., T., 2019. caret: Classification and Regression Training. [https://cran.r-
826 project.org/package=caret](https://cran.r-project.org/package=caret)

827 Kuhn, S., Cracknell, M.J., Reading, A.M., 2018. Lithologic mapping using Random Forests
828 applied to geophysical and remote-sensing data: A demonstration study from the Eastern
829 Goldfields of Australia. *Geophysics* 83, B183–B193. <https://doi.org/10.1190/geo2017-0590.1>

830 Leveridge, B.E., Hartley, A.J., 2006. The Varisan Orogeny: the development and deformation
831 of Devonian/Carboniferous basins in SW England and South Wales, in: Brenchley, P.J.,
832 Rawson, P.F. (Eds.), *The Geology of England and Wales*. The Geological Society, London, pp.
833 225–256.

834 Manning, D.A.C., Hill, P.I., 1990. The petrogenetic and metallogenetic significance of topaz
835 granite from the southwest England orefield. *Geological Society of America Special Paper*
836 246, 51–69.

837 Mellor, A., Boukir, S., Haywood, A., & Jones, S. (2015). Exploring issues of training data
838 imbalance and mislabelling on random forest performance for large area land cover
839 classification using the ensemble margin. *ISPRS Journal of Photogrammetry and Remote
840 Sensing*, 105, 155–168. <https://doi.org/10.1016/j.isprsjprs.2015.03.014>

841 Moore, J.M., Camm, S., 1982. Interactive enhancement of Landsat Imagery for structural
842 mapping in tin-tungsten prospecting: a case history of the S.W. England Orefield (U.K.), in:

843 International Symposium on Remote Sensing of Environment, Second Thematic Conference,
844 Remote Sensing for Exploration Geology. Fort Worth, Texas, December 6 - 10, 1982, pp.
845 727–740.

846 Moore, J.M., Jackson, N., 1977. Structure and mineralization in the Cligga granite stock,
847 Cornwall. *Journal of the Geological Society, London* 133, 467–480.
848 <https://doi.org/10.1144/gsjgs.133.5.0467>

849 Moscati, R. J., & Neymark, L. A. (2020). U–Pb geochronology of tin deposits associated with
850 the Cornubian Batholith of southwest England: Direct dating of cassiterite by in situ LA-
851 ICPMS. *Mineralium Deposita*, 55(1), 1–20. <https://doi.org/10.1007/s00126-019-00870-y>

852 Müller, A., Seltmann, R., Halls, C., Siebel, W., Dulski, P., Jeffries, T., Spratt, J., Kronz, A., 2006.
853 The magmatic evolution of the Land’s End pluton, Cornwall, and associated pre-enrichment
854 of metals. *Ore Geology Reviews* 28, 329–367.
855 <https://doi.org/10.1016/j.oregeorev.2005.05.002>

856 Newall, P.S., 1994. An integrated geochemical approach to investigate the concealed
857 mineralization at the Redmoor Sn/W sheeted vein deposit, east Cornwall, England. *Journal*
858 *of Southeast Asian Earth Sciences* 10, 109–130. [https://doi.org/10.1016/0743-](https://doi.org/10.1016/0743-9547(94)90013-2)
859 [9547\(94\)90013-2](https://doi.org/10.1016/0743-9547(94)90013-2)

860 Newall, P.S., Newall, G.C., 1989. Use of litho-geochemistry as an exploration tool at Redmoor
861 sheeted-vein complex, east Cornwall, southwest England. *Transactions of the Institution of*
862 *Mining and Metallurgy* 98, B162–B174.

863 Nykänen, V., 2008. Radial Basis Functional Link Nets Used as a Prospectivity Mapping Tool
864 for Orogenic Gold Deposits Within the Central Lapland Greenstone Belt, Northern
865 Fennoscandian Shield. *Natural Resources Research* 17, 29–48.
866 <https://doi.org/10.1007/s11053-008-9062-0>

867 Nykänen, V., Lahti, I., Niiranen, T., Korhonen, K., 2015. Receiver operating characteristics
868 (ROC) as validation tool for prospectivity models - A magmatic Ni-Cu case study from the
869 Central Lapland Greenstone Belt, Northern Finland. *Ore Geology Reviews* 71, 853–860.
870 <https://doi.org/10.1016/j.oregeorev.2014.09.007>

871 Nykänen, V., Niiranen, T., Molnhár, F., Lahti, I., Korhonen, K., Cook, N., Skyttä, P., 2017.
872 Optimizing a Knowledge-driven Prospectivity Model for Gold Deposits Within Peräpohja
873 Belt, Northern Finland. *Natural Resources Research* 26, 571–584.
874 <https://doi.org/10.1007/s11053-016-9321-4>

875 O’Brien, J. J., Spry, P. G., Nettleton, D., Xu, R., & Teale, G. S. (2014). Using Random Forests to
876 distinguish gahnite compositions as an exploration guide to Broken Hill-type Pb-Zn-Ag
877 deposits in the Broken Hill domain, Australia. *Journal of Geochemical Exploration*, 149, 74–
878 86. <https://doi.org/10.1016/j.gexplo.2014.11.010>

879 Rattey, P.R., Sanderson, D.J., 1984. The structure of SW Cornwall and its bearing on the
880 emplacement of the Lizard Complex. *Journal of the Geological Society, London* 141, 87–95.

881 R Core Team, 2019. R: A Language and Environment for Statistical
882 Computing. <https://www.r-project.org>

883 Robinson, G.R., Larkins, P.M., 2007. Probabilistic prediction models for aggregate quarry
884 siting. *Natural Resources Research* 16, 135–146. [https://doi.org/10.1007/s11053-007-9039-](https://doi.org/10.1007/s11053-007-9039-4)
885 4

886 Rodriguez-Galiano, V., Sanchez-Castillo, M., Chica-Olmo, M., Chica-Rivas, M., 2015. Machine
887 learning predictive models for mineral prospectivity: An evaluation of neural networks,
888 random forest, regression trees and support vector machines. *Ore Geology Reviews* 71,
889 804–818. <https://doi.org/10.1016/j.oregeorev.2015.01.001>

890 Sanderson, D.J., Dearman, W.R., 1973. Structural zones of the Variscan fold belt in SW
891 England, their location and development. *Journal of the Geological Society, London* 129,
892 527–536. <https://doi.org/10.1144/gsjgs.129.5.0527>

893 Schetselaar, E., 2002. Petrogenetic interpretation from gamma-ray spectrometry and
894 geological data: the Arch Lake zoned peraluminous granite intrusion, Western Canadian
895 shield. *Exploration Geophysics* 33, 35–43. <https://doi.org/10.1071/EG02035>

896 Scrivener, R.C., 2006. Cornubian granites and mineralization of SW England, in: Brenchley,
897 P.J., Rawson, P.F. (Eds.), *The Geology of England and Wales*. The Geological Society, London,
898 pp. 257–268.

899 Shail, R.K., Alexander, A.C., 1997. Late Carboniferous to Triassic reactivation of Variscan
900 basement in the western English Channel: evidence from onshore exposures in south
901 Cornwall. *Journal of the Geological Society, London* 154, 163–168.
902 <https://doi.org/10.1144/gsjgs.154.1.0163>

903 Shail, R.K., Leveridge, B.E., 2009. The Rhenohercynian passive margin of SW England:
904 Development, inversion and extensional reactivation. *Comptes Rendus Geoscience* 341,
905 140–155.

906 Shail, R.K., Wilkinson, J.J., 1994. Late-to Post-Variscan extensional tectonics in south
907 Cornwall. *Proceedings of the Ussher Society* 8, 262–270.

908 Shail, R., McFarlane, J., Hassall, L., Thiel, H., Stock, T., Smethurst, M., Tapster, S., Scrivener,
909 R., Leveridge, B., Simons, B., 2017. The geological setting of the Hemerdon W–Sn deposit.
910 *Transactions of the Institutions of Mining and Metallurgy, Section B: Applied Earth Science*
911 7453, 1. <https://doi.org/10.1080/03717453.2017.1306292>

912 Simons, B., Andersen, J.C., Shail, R.K., Jenner, F., 2017. Fractionation of Li, Be, Ga, Nb, Ta, In,
913 Sn, Sb, W and Bi in the peraluminous Early Permian Variscan granites of the Cornubian
914 Batholith: precursor processes to magmatic-hydrothermal mineralisation. *Lithos* 278-281,
915 491–512. <https://doi.org/10.1016/j.lithos.2017.02.007>

916 Simons, B., Shail, R.K., Andersen, J.C., 2016. The petrogenesis of the Early Permian Variscan
917 granites of the Cornubian Batholith: Lower plate post-collisional peraluminous magmatism
918 in the Rhenohercynian Zone of SW England. *Lithos* 260, 76–94.
919 <https://doi.org/10.1016/j.lithos.2016.05.010>

920 Smith, M., Banks, D.A., Yardley, B.W. and Boyce, A., 1996. Fluid inclusion and stable isotope
921 constraints on the genesis of the Cligga Head Sn-W deposit, SW England. *European Journal*
922 *of Mineralogy*, pp.961-974

- 923 Sukumar, M., Venkatesan, N., Babu, C.N.K., 2014. A review of various lineament detection
924 techniques for high resolution satellite images. *International Journal of Advanced Research*
925 *in Computer Science and Software Engineering* 4, 72–78.
- 926 Sun, T., Chen, F., Zhong, L., Liu, W., Wang, Y., 2019. GIS-based mineral prospectivity mapping
927 using machine learning methods: a case study from Tongling ore district, eastern China. *Ore*
928 *Geology Reviews* 109, 26–49. <https://doi.org/10.1016/j.oregeorev.2019.04.003>
- 929 Tapster, S. R. and Bright, J. W. G.: High-precision ID-TIMS Cassiterite U-Pb systematics using
930 a low-contamination hydrothermal decomposition: implications for LA-ICP-MS and ore
931 deposit geochronology, *Geochronology Discuss.*, <https://doi.org/10.5194/gchron-2019-22>,
932 in review, 2020
- 933 Wang, C., Rao, J., Chen, J., Ouyang, Y., Qi, S., Li, Q., 2017a. Prospectivity mapping for “Zhuxi-
934 type” copper-tungsten polymetallic deposits in the Jingdezhen region of Jiangxi Province,
935 South China. *Ore Geology Reviews* 89, 1–14.
936 <https://doi.org/10.1016/j.oregeorev.2017.05.022>
- 937 Wang, J., Zuo, R., Caers, J., 2017b. Discovering geochemical patterns by factor-based cluster
938 analysis. *Journal of Geochemical Exploration* 181, 106–115.
939 <https://doi.org/10.1016/j.gexplo.2017.07.006>
- 940 Wang, W., Cheng, Q., Zhang, S., Zhao, J., 2018. Anisotropic singularity: A novel way to
941 characterize controlling effects of geological processes on mineralization. *Journal of*
942 *Geochemical Exploration* 189, 32–41. <https://doi.org/10.1016/j.gexplo.2017.07.019>
- 943 Willis-Richards, J., Jackson, N.J., 1989. Evolution of the Cornubian Ore Field, Southwest
944 England: Part I. Batholith Modeling and Ore Distribution. *Economic Geology* 84, 1078–1100.
- 945 Witten, I.H., Frank, E., Hall, M.A., Pal, C.J., 2017. *Data Mining: Practical Machine Learning*
946 *Tools and Techniques*, Fourth. ed. Morgan Kaufmann (Elsevier).
- 947 Wragg, J., Cave, M., Hamilton, E., Lister, T., 2018. The Link between Soil Geochemistry in
948 South-West England and Human Exposure to Soil Arsenic. *Minerals* 8, 570.
949 <https://doi.org/10.3390/min8120570>
- 950 Yeomans, C.M., Middleton, M., Shail, R.K., Grebby, S., Lusty, P.A.J., 2019. Integrated Object-
951 Based Image Analysis for semi-automated geological lineament detection in southwest
952 England. *Computers & Geosciences* 123, 137–148 [Available Online November 2018].
953 <https://doi.org/10.1016/j.cageo.2018.11.005>
- 954 Zadeh, L.A., 1965. Fuzzy sets. *Information and Control* 8, 338–353.
955 [https://doi.org/10.1016/S0019-9958\(65\)90241-X](https://doi.org/10.1016/S0019-9958(65)90241-X)
- 956 Zhao, J., Zuo, R., Chen, S., Kreuzer, O.P., 2015. Application of the tectono-geochemistry
957 method to mineral prospectivity mapping: A case study of the Gaosong tin-polymetallic
958 deposit, Gejiu district, SW China. *Ore Geology Reviews* 71, 719–734.
959 <https://doi.org/10.1016/j.oregeorev.2014.09.023>

960

961 **Figure Captions**

962 *Figure 1: Summary geology of SW England showing Devonian-Carboniferous sedimentary*
963 *host rock in grey, granite outcrop in red and depth-to granite contours based on the granite*
964 *surface model by Willis-Richards and Jackson (1989). Black lines represent regional*
965 *lineaments derived by Yeomans et al. (2019) from Tellus South West airborne geophysical*
966 *data.*

967 *Figure 2: Schematic illustrations of the kinematics and structures generated during Permian-*
968 *Triassic extension (D3-D6). After Shail and Alexander (1997).*

969 *Figure 3: Schematic outline of extractive areas in SW England showing tin, copper and*
970 *tungsten. Data from BGS GeoIndex (2018) are based on historic production values from*
971 *known mines, deposit and prospect localities as well as reported mineral showings and*
972 *panned concentrates. Important tungsten producers are labeled based on data from Dines*
973 *(1956) and Jackson et al. (1989). Key mining areas are highlighted on the map: a = St Just, b*
974 *= Camborne-Redruth, c = Breage, d = St Austell, e = Bodmin, f = Tamar Valley.*

975 *Figure 4: Mineral prospectivity modelling workflow for combining knowledge-based feature*
976 *extraction into a data-driven machine learning approach to generate spatially refined and*
977 *robust targets for mineral exploration.*

978 *Figure 5: Conceptual deposit model for tungsten mineralisation in SW England showing the*
979 *main geological phenomena targeted by the prospectivity modelling.*

980 *Figure 6: Granite geochemistry showing the distribution of granite types based on the*
981 *classification by Simons et al. (2016). The G2 granite is distinct having a low Zr/Eu ratio and*
982 *high K, however, the G1a granite shows a similar signature.*

983 *Figure 7: (A) interpolated stream-sediment geochemical data for tungsten that have been*
984 *transformed using the fuzzy membership function. (B) interpolated soil geochemical data for*
985 *tungsten that have been transformed using the fuzzy membership function. (C) resulting*
986 *tungsten geochemical data that have been combined using the fuzzyOR operator to*
987 *emphasis key anomalies.*

988 *Figure 8: Schematic Random Forest diagram illustrating the interaction of decision trees in*
989 *determining a classification value. Where randomly generated trees attempt to resolve the*
990 *class value for a single instance through a majority vote system based on the leaf nodes*
991 *(based on Belgiu & Drăguț, 2016).*

992 *Figure 9: (A) Classification map (B) Class probability map and (C) confidence map for the*
993 *standardised variables Random Forest prospectivity model. Classes show the two class*
994 *scenario where 1 is unprospective and 2 is prospective. The class probability and confidence*
995 *models are categorised to show 0.9 to 1 as highly favourable (red), 0.8 to 0.9 as favourable*
996 *(amber), 0.65 to 0.8 as less favourable (turquoise), 0.5 to 0.65 as possibly favourable (blue)*
997 *and <0.5 as unfavourable (grey).*

998 *Figure 10: (A) Classification map (B) Class probability map and (C) confidence map for the*
999 *fuzzy-transformed variables Random Forest prospectivity model. Classes show the two class*
1000 *scenario where 1 is unprospective and 2 is prospective. The class probability and confidence*
1001 *models are categorised to show 0.9 to 1 as highly favourable (red), 0.8 to 0.9 as favourable*
1002 *(amber), 0.65 to 0.8 as less favourable (turquoise), 0.5 to 0.65 as possibly favourable (blue)*
1003 *and <0.5 as unfavourable (grey).*

1004 *Figure 11: Key target locations based on the class probability map from the fuzzy-*
1005 *transformed variables model. The Breage district is shown in (A) where drilling projects and*
1006 *mining legacy data are shown to validate the targets. Targets around the Bodmin Granite*
1007 *are shown in (B) with new areas validated by a drilling report. The eastern margin of the*
1008 *Dartmoor Granite is shown in (C) where mining legacy data are proximal to favourable*
1009 *targets.*

1010

1011 **Table Captions**

1012 *Table 1: Geochemical data included as evidence for tungsten mineralisation. The*
1013 *geochemistry are grouped into three phenomena describing the mineralisation, granite*
1014 *aureole and granite type.*

1015 *Table 2: AUC values for evidence layers transformed using fuzzy membership functions. The*
1016 *AUC values are calculated from ten ROC curve analyses using randomly generated false*
1017 *occurrences.*

1018 *Table 3: AUC values for combined geochemical elements and ratios, calculated from ten ROC*
1019 *curve analyses using randomly generated false occurrences. These are compared to the*
1020 *geochemical values for original datasets from soil and stream-sediment (SS) data. In some*
1021 *cases (W, Sn, As, Na) the combination is mutually beneficial.*

1022 *Table 4: AUC values for each Random Forest™ prospectivity model. Calculated from ten ROC*
1023 *curve analyses using randomly generated false occurrences. The key parameters have been*
1024 *included for each model.*

1025 *Table 5: Area assessment for both standardised and fuzzy-transformed models. The data*
1026 *have been calculated in a GIS to show the area accounted for by each class as a sum and a*
1027 *percentage for both the class probability (Prob) map and confidence (Conf) maps. Small*
1028 *discrepancies are attributed to rounding errors.*

Figure 1

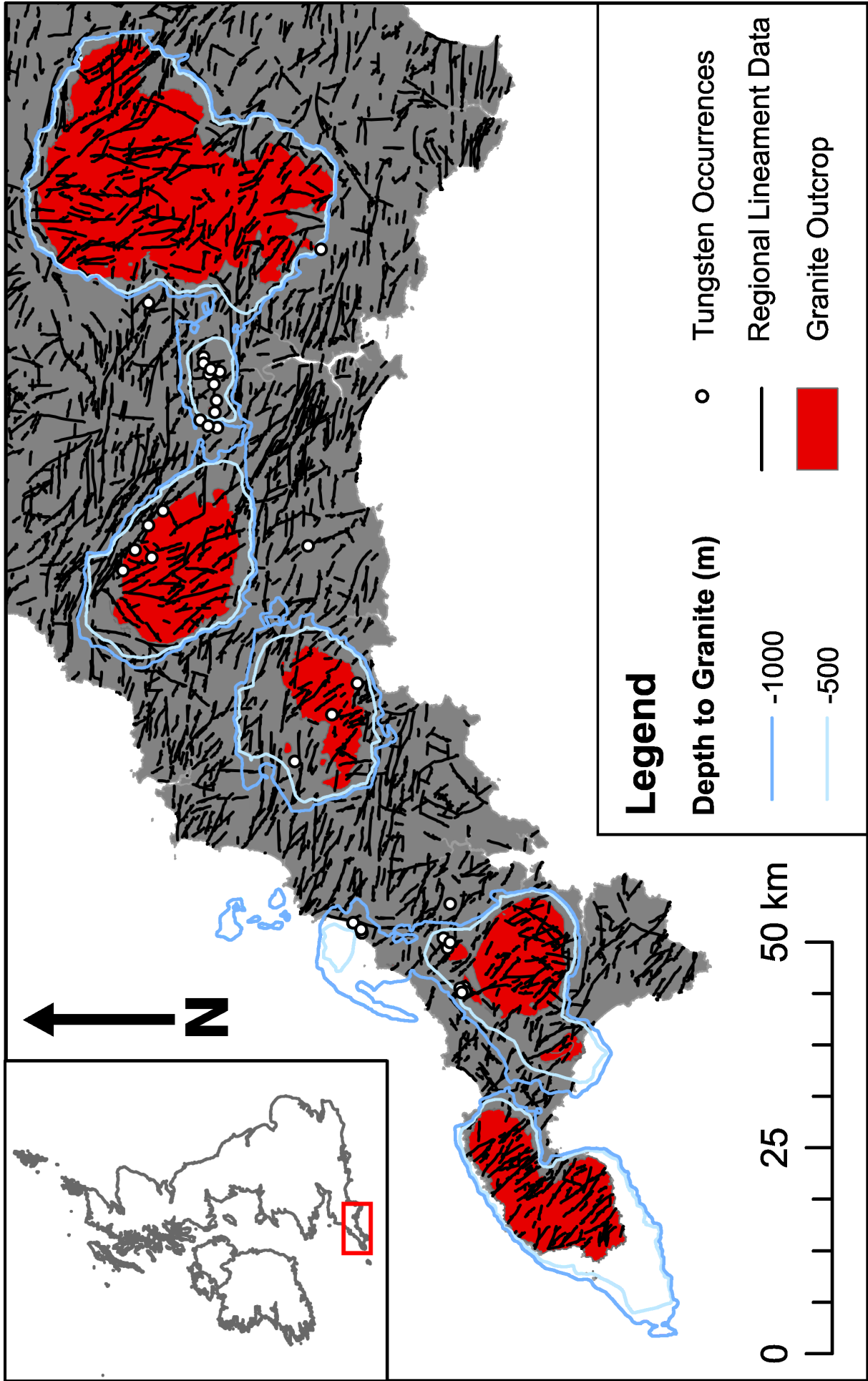


Figure 2

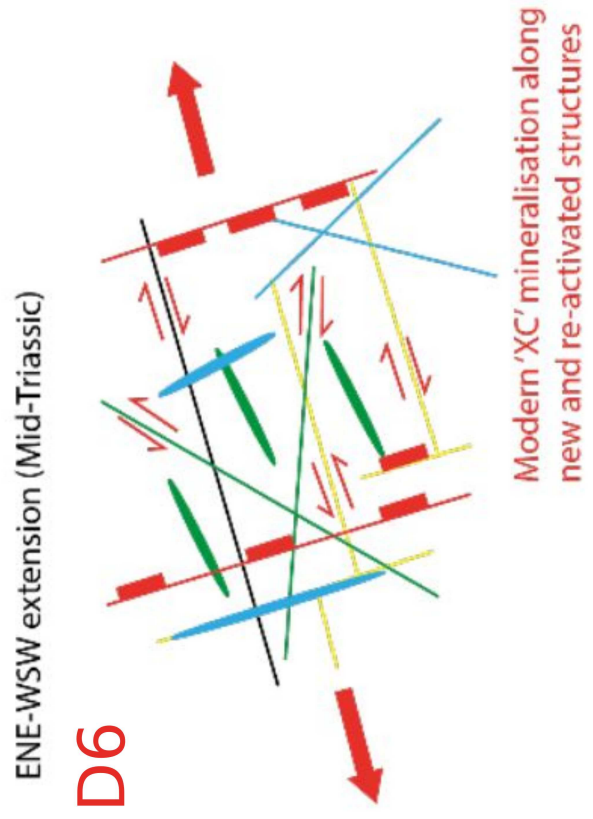
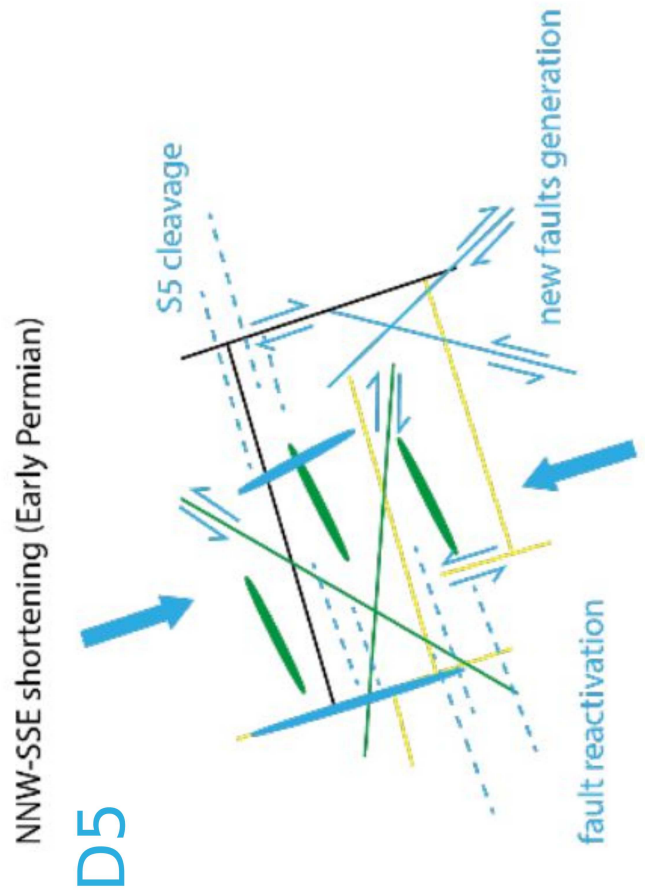
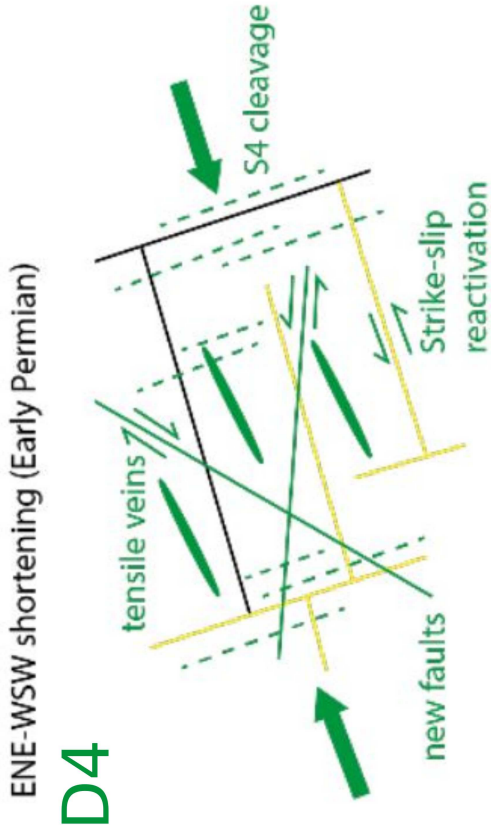
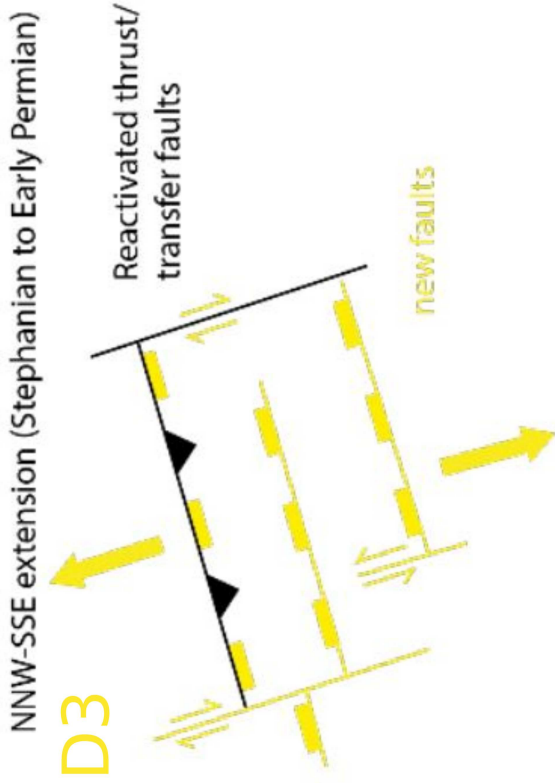


Figure 3

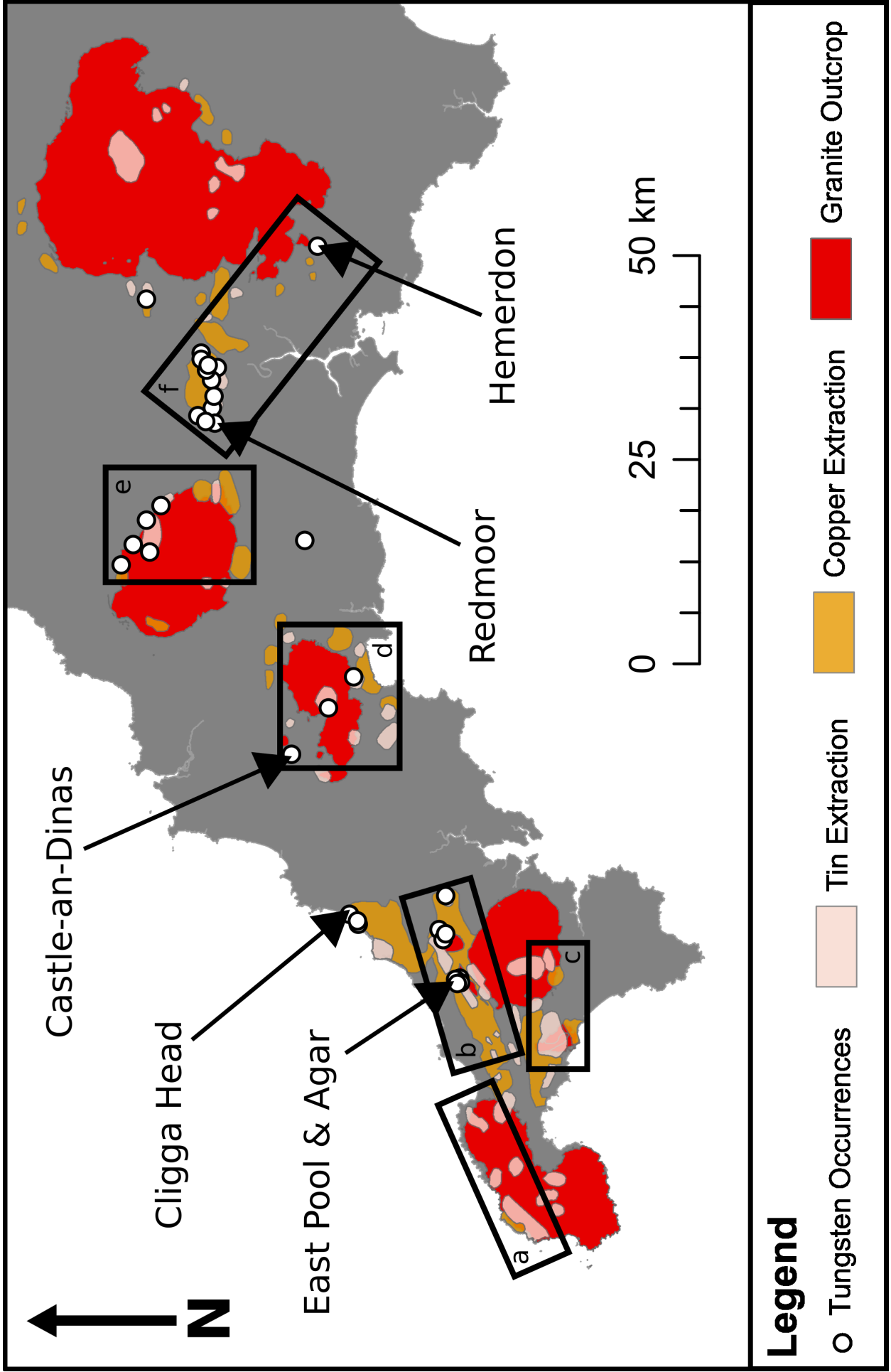


Figure 4

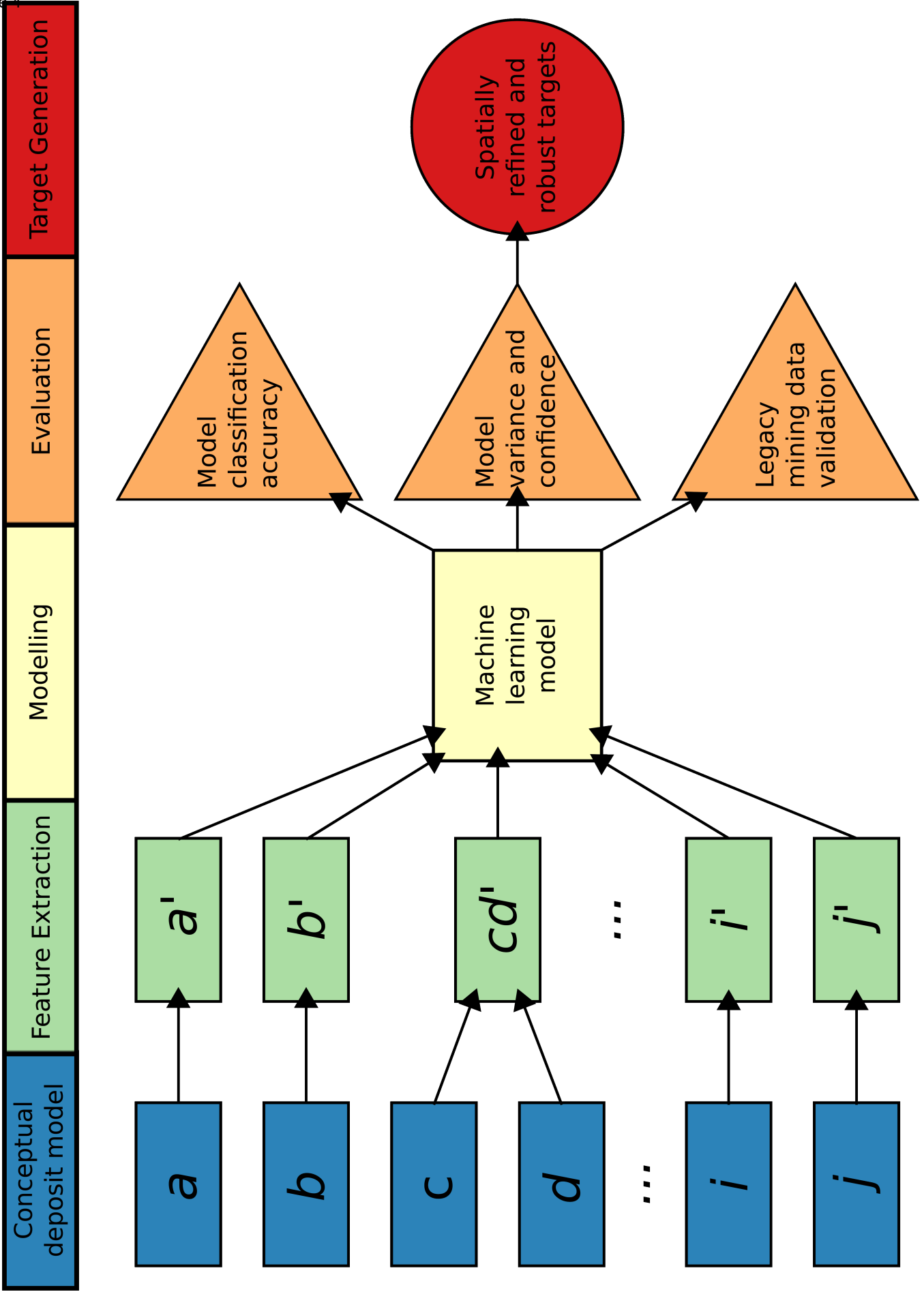


Figure 5

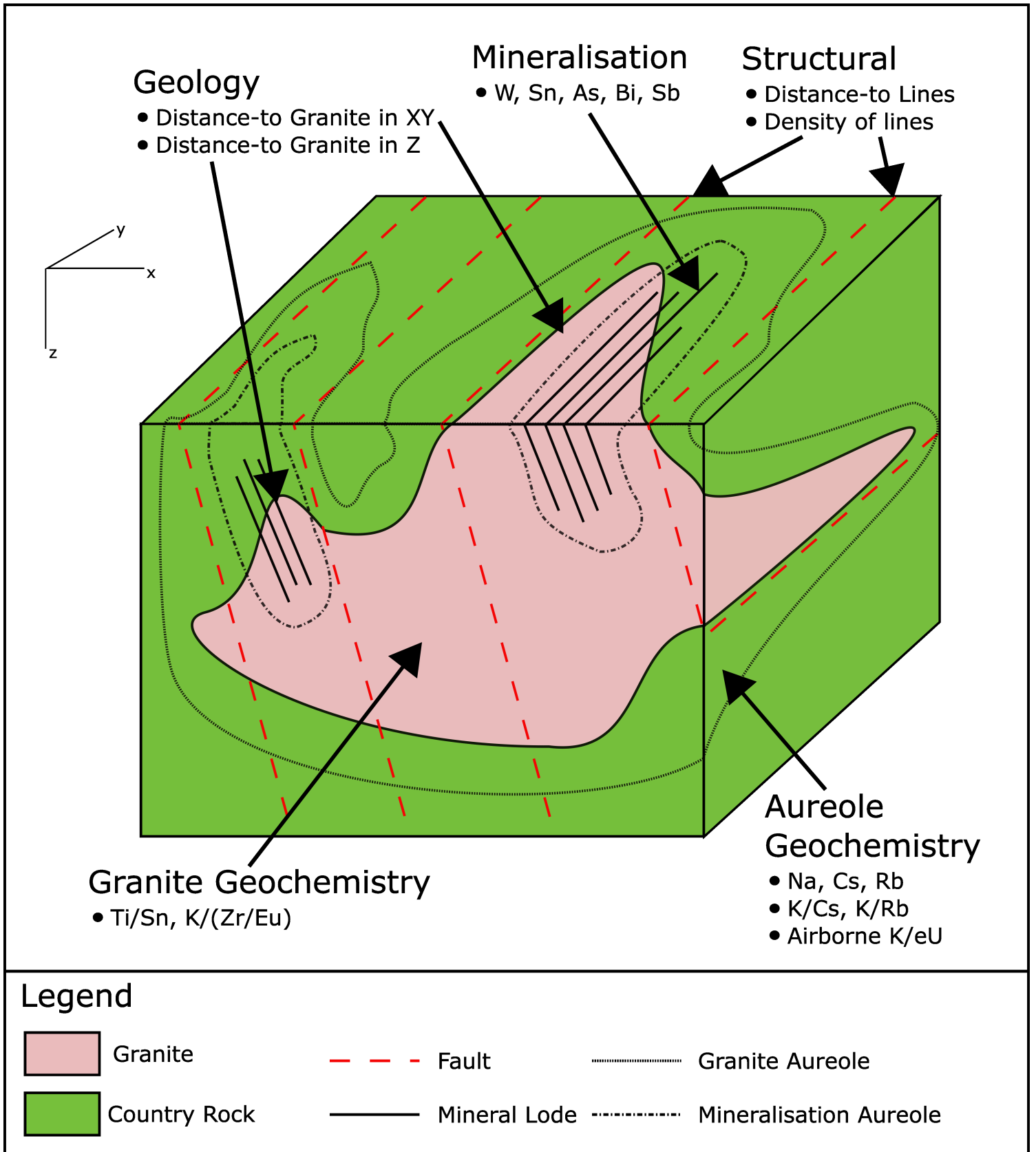


Figure 6

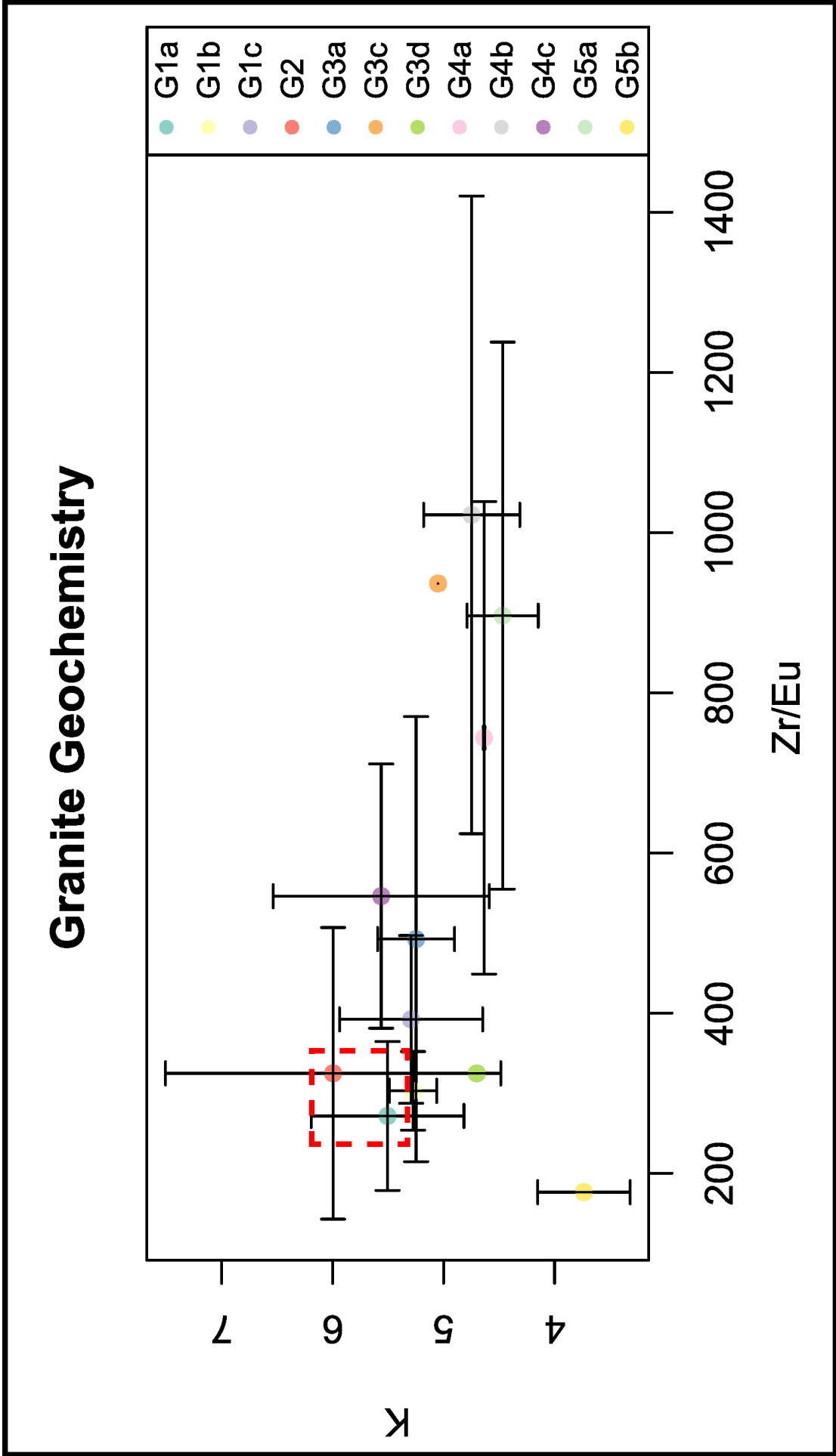


Figure 7

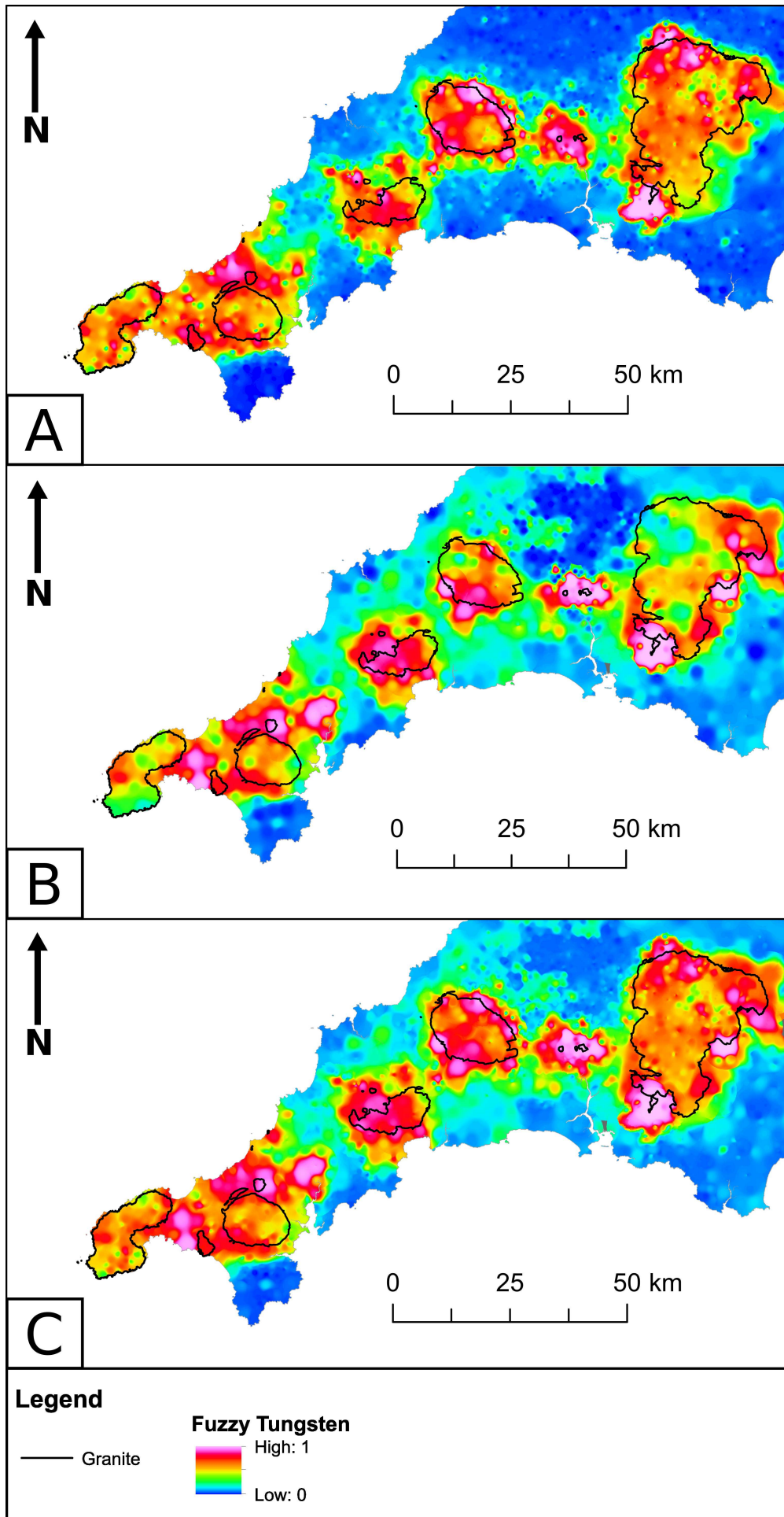


Figure 8

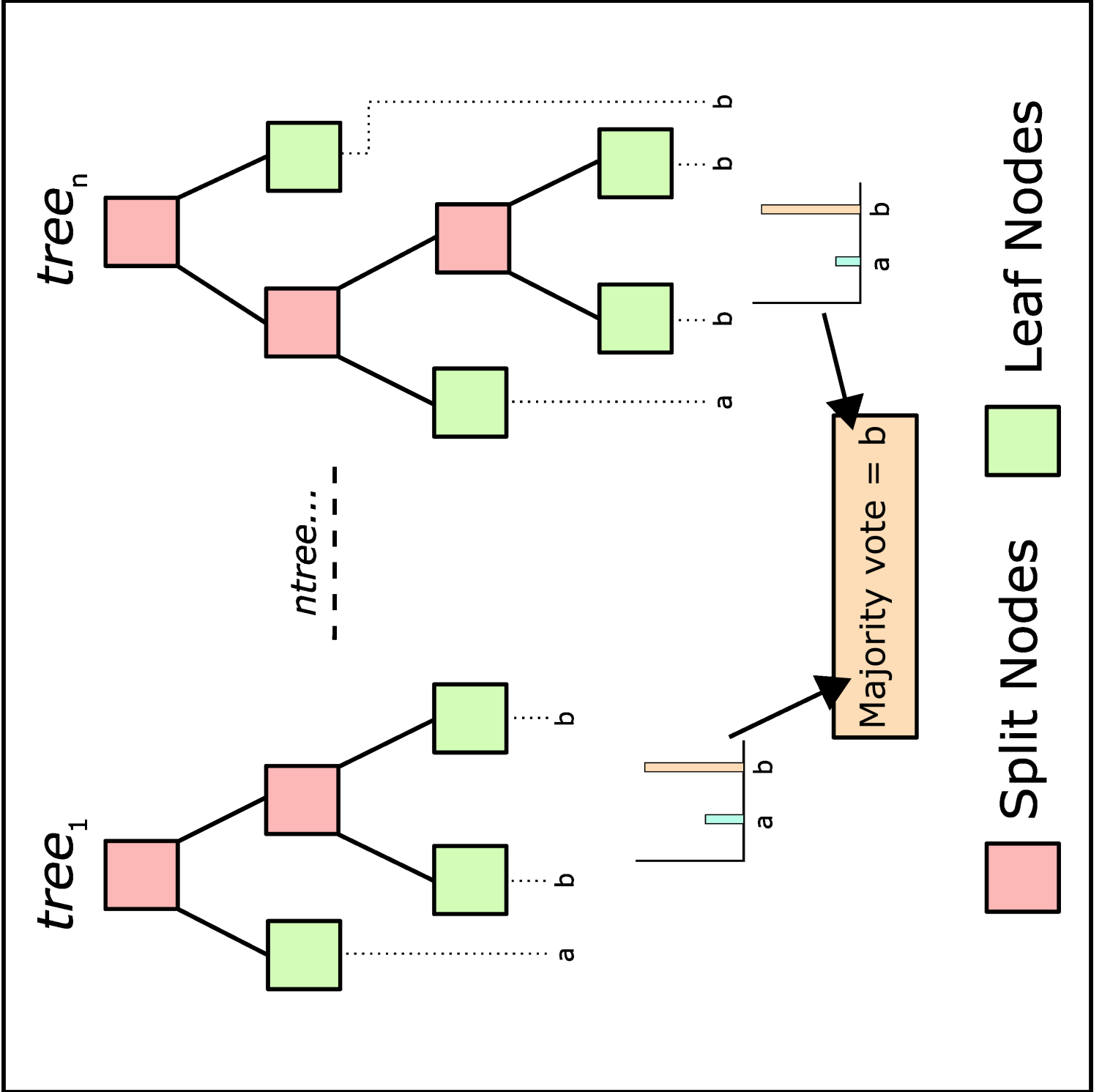


Figure 9

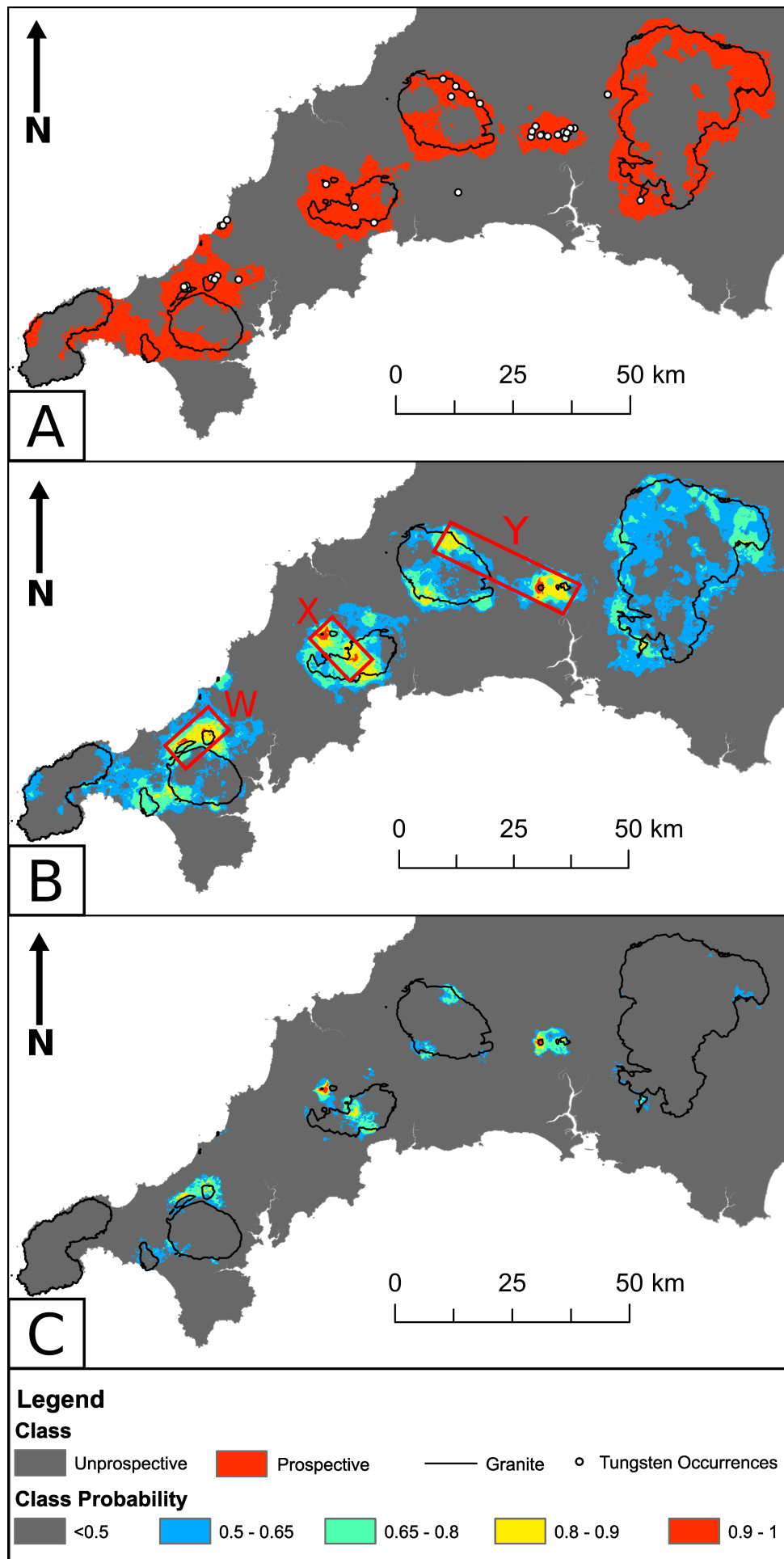


Figure 10

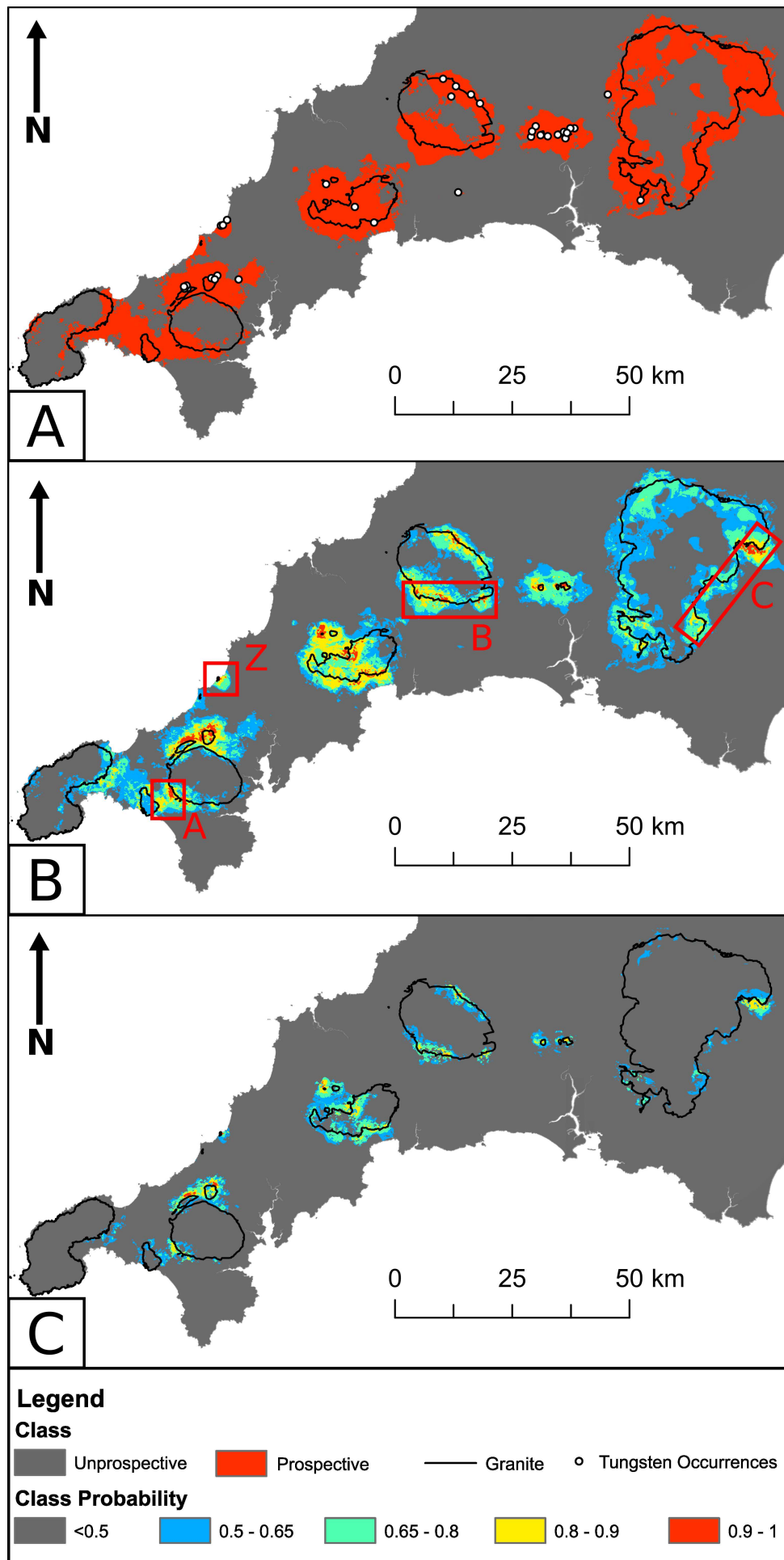


Figure 11

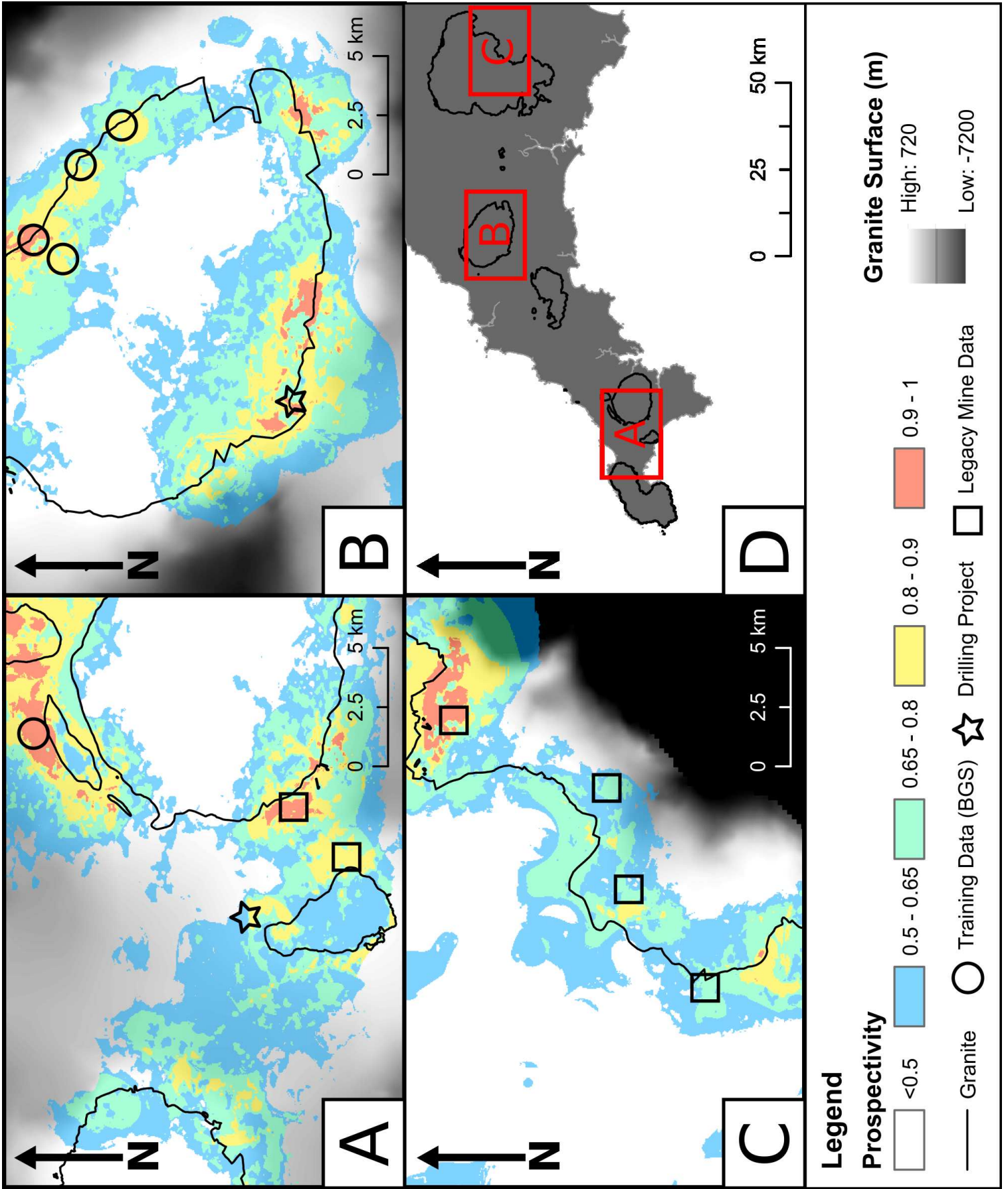


Table 1

Phenomenon	Elements	Sources
Mineralisation	W, Sn, As, Bi, Sb	(Andrews et al., 1987; Ball et al., 2002; Newall, 1994; Newall and Newall, 1989)
Aureole Alteration	Rb, Cs, Na*, K/Rb*, K/Cs*, K/eU*	(Ball et al., 1984, 1998; Newall, 1994; Newall and Newall, 1989)
Granite Composition	Ti/Sn*, K/(Zr/Eu)	(Ball et al., 1984, 1998; Simons et al., 2016)

Table 2

Evidence Layer	Midpoint	Spread	Func.	Mean	SD
Proximity-to Granite in Z	N/A	N/A	TOC	0.814	0.039
Proximity-to Granite in XY	2750	2	Small	0.887	0.03
Density all lines	0.478	4	Large	0.638	0.062
Proximity-to lines	2713.41	2	Small	0.577	0.055
Airborne K/eU ratio	0.7	10	Small	0.666	0.055
Geochem Soil W	7.08	2	Large	0.887	0.032
Geochem Soil Sn	57.57	3	Large	0.829	0.034
Geochem Soil As	55.08	2	Large	0.819	0.038
Geochem Soil Bi	1.4	2	Large	0.819	0.032
Geochem Soil Sb	2.83	2	Large	0.49	0.052
Geochem Soil Rb	159.46	3	Large	0.708	0.051
Geochem Soil Cs	16.36	3	Large	0.749	0.035
Geochem Soil Na	0.83	6	Small	0.701	0.057
Geochem Soil K/Cs	0.22	3	Small	0.764	0.029
Geochem Soil K/Rb	0.02	5	Small	0.751	0.051
Geochem Soil Ti/Sn	0.08	2	Small	0.824	0.037
Geochem Stream-sediment W	27.47	1	Large	0.874	0.031
Geochem Stream-sediment Sn	636.63	1	Large	0.722	0.057
Geochem Stream-sediment As	117.68	1	Large	0.824	0.032
Geochem Stream-sediment Bi	2.86	2	Large	0.809	0.032
Geochem Stream-sediment Sb	2.69	1	Large	0.594	0.036
Geochem Stream-sediment Rb	176.41	4	Large	0.644	0.045
Geochem Stream-sediment Cs	20.35	3	Large	0.69	0.047
Geochem Stream-sediment Na	6359.1	5	Small	0.709	0.052
Geochem Stream-sediment K/Cs	1813	3	Small	0.533	0.042
Geochem Stream-sediment K/Rb	157.63	5	Small	0.668	0.058
Geochem Stream-sediment Ti/Sn	387.78	2	Small	0.706	0.064
Geochem Stream-sediment K/(Zr/Eu)	136.02	2	Small	0.739	0.044

Table 3

Element or Ratio	Func.	Mean	SD	Soil	SS	Improvement in AUC
W	OR	0.901	0.026	0.887	0.874	INCREASE
Sn	OR	0.816	0.034	0.829	0.722	INCREASE
As	OR	0.851	0.033	0.819	0.824	INCREASE
Bi	OR	0.819	0.032	0.819	0.809	NO CHANGE
Sb	OR	0.537	0.085	0.49	0.594	DECREASE
Rb	OR	0.657	0.13	0.708	0.644	DECREASE
Cs	OR	0.71	0.037	0.749	0.69	DECREASE
Na	OR	0.758	0.048	0.701	0.709	INCREASE
K/Cs	OR	0.676	0.04	0.764	0.533	DECREASE
K/Rb	OR	0.713	0.055	0.751	0.668	DECREASE
Ti/Sn	OR	0.724	0.061	0.824	0.706	DECREASE

Table 4

Model Type	Input Layers	Key Parameters	Mean	SD
Random Forest (standardised variables)	All evidence layers with zero mean and equal variance	mtry = 5; ntree = 20 000	0.959	0.03
Random Forest (fuzzy-transformed variables)	All fuzzy evidence layers, including geochemical data merged using the <i>fuzzy OR</i> operator	mtry = 4; ntree = 20 000	0.96	0.04

Table 5

Class	Fuzzy-transformed model				Standardised model			
	Σ Prob	Prob (%)	Σ Conf	Conf (%)	Σ Prob	Prob (%)	Σ Conf	Conf (%)
<0.5	4597.3	76.58	5693.2	94.83	4526.6	75.4	5811.73	96.81
0.5-0.65	723.88	12.06	174.02	2.9	969.72	16.15	106.61	1.78
0.65-0.8	460.3	7.67	104.73	1.74	386.5	6.44	67.89	1.13
0.8-0.9	188.33	3.14	28.74	0.48	108.59	1.81	14.1	0.23
0.9-1.0	33.67	0.56	2.82	0.05	12.07	0.2	3.21	0.05
Total	6003.47	100	6003.52	100	6003.47	100	6003.54	100

Supplementary Information



Click here to access/download
e-component
Supplementary_Information.pdf



Declaration of Interest Statement

Declaration of interests

The authors declare that they have no known competing financial interests or personal relationships that could have appeared to influence the work reported in this paper.

The authors declare the following financial interests/personal relationships which may be considered as potential competing interests:

Nothing to declare